1 2 90

UNIVERSIDADE DE
COIMBRA

Ana Beatriz Pedro Fontes

Ab Initio Studies of Bi_2Se_3, Bi_2Te_3 and $Bi_2Se_{3-x}Te_x$

VOLUME 1

Dissertação no âmbito do Mestrado em Física com Especialização em Física da Matéria Condensada orientada pelo Doutor Pedro Borlido e pelo Professor Doutor Fernando Nogueira e apresentada ao Departamento de Física da Faculdade de Ciências e Tecnologias da Universidade de Coimbra

Setembro de 2022

Ab Initio Studies of Bi_2Se_3, Bi_2Te_3 and $Bi_2Se_{3-x}Te_x$

Ana Beatriz Pedro Fontes

Supervisor: Dr. Pedro Borlido
Prof. Fernando Nogueira

A thesis submitted for the degree of
Master in Physics

Department of Physics of the Faculty of Sciences and Technology
University of Coimbra

September 2022

Agradecimentos

Em primeiro lugar, deixo o meu profundo agradecimento ao Dr. Pedro Borlido por todo o acompanhamento dado, ao longo deste ano, e pela disponibilidade para esclarecer dúvidas e resolver problemas que foram surgindo. Agradeço também ao Prof. Dr. Fernando Nogueira pela orientação dada, pela revisão teórica da tese e incentivo no prosseguimento dos estudos.

Em segundo lugar, queria agradecer aos meus pais e à minha irmã por todo o apoio e incentivo dado, fundamental para chegar aqui.

Em terceiro lugar, agradeço ao meu namorado, Leonardo Kleman, por toda a compreensão, apoio emocional e por me incentivar a seguir os meus sonhos.

Por último, queria agradecer à Ana e à Valéria por estarem sempre lá para mim.

Abstract

Topological insulators are materials with an energy gap in the bulk but with topologically protected conducting surface states. These materials have garnered a lot of attention due to their potential usefulness in, e.g., spintronics. The bismuth chalcogenides are an extensively studied family of topological insulators, with $\mathrm{Bi_2Se_3}$ as a prototypical material, given its relatively simple surface states and its almost ideal Dirac cone. $\mathrm{Bi_2Te_3}$ is also one of the best thermoelectrical materials for applications near room temperature. However, its performance is limited by thermally generated carriers due to the small energy band gap. The substitution of tellurium atoms with selenium, a process named alloying, increases the energy band gap but leads to different transport properties. Although $\mathrm{Bi_2Se_3}$ and $\mathrm{Bi_2Te_3}$ have been extensively studied, most of the electronic structure's calculations are done with experimental structures without full geometry optimisation of the crystal structure. We use different exchange and correlation functionals to calculate the band structure of $\mathrm{Bi_2Se_3}$ and $\mathrm{Bi_2Te_3}$ using optimised structures. Using the Local Density Approximation exchange and correlation functional, with the D2 van der Waals corrections, we study the substitutional alloy $\mathrm{Bi_2Se_{3-x}Te_x}$. Starting from ab-initio calculations of small inequivalent supercell configurations, we estimate the density of states, the lattice parameters, and the energy gap as a function of the concentration of tellurium.

Keywors: Topological insulators, Density Functional Theory (DFT), alloy, ab-initio, configuration.

Resumo

Os isoladores topológicos são materiais com um hiato de energia (band gap) no seu interior mas que apresentam estados condutores na superfície, topológicamente protegidos. Estes materiais receberam muita atenção devido à sua potencial aplicabilidade, por exemplo, em spintrónica. Os dicalgogenóides de bismuto são uma família de isoladores topológicos extensivamente estudados que tem o Bi_2Se_3 como material protótipo devido aos estados de superfície serem relativamente simples e ao cone de Dirac quase ideal. O Bi_2Te_3 é também um dos melhores materiais termoelétricos para aplicações próximo da temperatura ambiente. No entanto, a sua performance é limitada por transportadores de carga gerados termicamente devio ao hiato de energia reduzido. A substituição de átomos de telúrio por selénio (alloying) aumenta o hiato de energia mas leva a diferentes propriedades de transporte. Apesar do Bi_2Se_3 e do Bi_2Te_3 terem sido extensivamente estudados, a maioria dos cálculos de estrutura eletrónica são feitos utilizando as estruturas experimentais sem otimização da geometria da estrutura cristalina. Utilizámos diferentes funcionais de troca e correlação para determinar a estrutura de bandas do Bi_2Se_3 e Bi_2Te_3, utilizando estruturas otitimizadas. Usando a "Local Density Approximation" como funcional de troca e correlação, com as correções de van der Waals D2 de Grimme et al. estudámos a liga substitucional $Bi_2Se_{3-x}Te_x$. Partindo de cálculos ab-initio de configurações de supercélulas não equivalentes pequenas, estimámos a densidade de estados, os parâmetros da rede cristalina e o hiato de energia em função da concentração de telúrio.

Palavras-chave: Isolador topológico, Teoria do Funcional da Densidade (DFT), liga, ab-initio, configuração.

Table of contents

List of figures

List of tables

Nomenclature

Acronyms / Abbreviations

2D	two-dimensional
3D	three-dimensional
BZ	Brillouin zone
CBM	conduction band minimum
CE	Cluster expansion
DFT	Density Functional Theory
GGA	Generalised Gradient Approximation
HK	Hohenberg-Kohn
KS	Kohn-Sham
LDA	Local Density Approximation
PBE	Perdew–Burke-Ernzerhof
SOC	spin-orbit coupling
TI	topological insulator
TR	time reversal
TRIM	time-reversal invariant momentum
VBM	valence band maximum
VCA	Virtual Crystal Approximation
vdW	van der Walls

Chapter 1

Introduction

1.1 Motivation

Topological insulators are materials with a band gap in the bulk as standard insulators but have protected conducting surface states on the sample's boundary.[2] These surface states are possible due to intrinsic spin-orbit interaction (SOC) and time-reversal symmetry.[1]

Bi_2Se_3 was theoretically predicted and confirmed experimentally to be one of the simplest 3D topological insulators with robust surface states consisting of a single Dirac cone at Γ point. It also has a large band gap of ≈ 0.3 eV, indicating that it can have a topological insulator behaviour at room temperature, making it attractive for potential applications in spintronics.[2][3]

Bi_2Te_3 is also a well-known topological insulator whose surface states exhibit valley degeneracy around Γ, deviating from the simple Dirac cone. Nevertheless, it is one of the best thermoelectrical materials for applications near room temperature. Its performance is limited by thermally generated carriers due to the small bandgap of 0.15 eV. Alloying it with Bi_2Se_3 increases the bandgap but leads to different thermal and electrical transport properties. A characterisation alloy's properties as a function of the concentration of Te is relevant.

Additionally, there is interest in the electronic structure of the substitutional alloys $Bi_2Se_{3-x}Te_x$ as they are also topological insulators.

Bismuth selenide, bismuth telluride and all intermediate alloys crystallise in a rhombohedral structure within the D_{3d}^5 (R$\bar{3}$m) space group.[4] But, they can also be visualised as a hexagonal unit cell with a layered structure, formed by quintuple layers of $X^{(1)} - Bi - X^{(2)} - Bi - X^{(1)}$ where the number in parentheses designates inequivalent chalcogen (X) sites (figure 1.1).

Although Bi_2Se_3 and Bi_2Te_3 have been extensively studied, most of the electronic structure's calculations are done with experimental structures without full geometry optimisation of the crystal structure. In this work, we use different exchange and correlation functionals to predict the bandstructure of Bi_2Se_3 and Bi_2Te_3 using optimised structures.

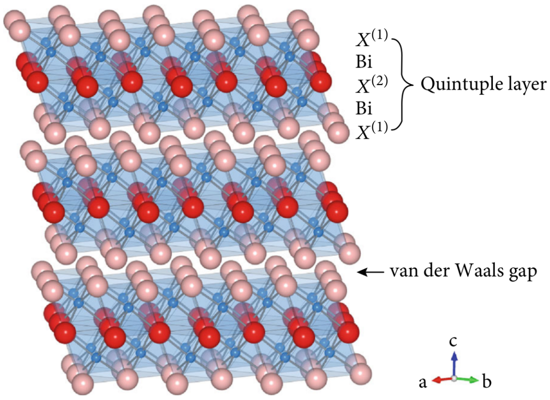

Fig. 1.1 The crystal structure of $Bi_2Se_{3-x}Te_x$ is composed of quintuple layers of X $X^{(1)} - Bi - X^{(2)} - Bi - X^{(1)}$ where X represents either Te or Se and the number in parentheses designates between the two inequivalent sites.[5]

Using Local Density Approximation exchange and correlation functional, with the D2 van der Waals corrections of Grimme et al.[6], we study the substitutional alloys $Bi_2Se_{3-x}Te_x$. For small inequivalent supercell configurations, we estimate the density of states, the lattice parameters, and the energy gap as a function of the concentration of Te.

1.2 Goals

The main objective of this thesis is to study the $Bi_2Se_{3-x}Te_x$ family of compounds. We want to investigate its electronic properties using the code Quantum ESPRESSO.[7][8] In particular, we intend to:

- Use different exchange and correlation functionals to predict the band structure of Bi_2Se_3 and Bi_2Te_3, two topological insulators with layered structures.
- Study mixing of these two materials (i.e. their alloys), to understand the evolution of their structural parameters, energy gap and density of states;
- Give insight on the experimental results of our colleagues in the CFisUC;
- Predict alloys properties (e.g. topological indices) as a function of the Te concentration.

1.3 Dissertation outline

The dissertation is structured as follows: **Chapter 2** is dedicated to an overview of the Density Functional Theory, the framework for all calculations we did. **Chapter 3** describes essential topology concepts in the context of topological insulators. In **Chapter 4**, an insight into how to model random substitutional alloys computationally is given. **Chapter 5** is reserved for the presentation and discussion of the results. Finally, in **Chapter 6**, the main results are summarized, and suggestions for future work are proposed.

Units and dimensions

We use a system of units convenient in atomic physics in this work. We will adopt the Hartree atomic units $\hbar = m_e = e = 4\pi/\epsilon_0 = 1$ in our equations to write them in the simplest form. Although, for the results, the preferred unit of length will be the angstrom, $\text{Å} = 1 \times 10^{-10}\text{m}$, and of energy will be the eV.

Chapter 2

Density Functional Theory

Density Functional Theory (DFT) is an exact approach used to investigate the ground-state electronic properties of quantum many-body systems.

The current formulation is based on Hohenberg and Kohn's [9] (1964) and Kohn and Sham's [10] (1965) papers. The first proves the existence of a density's functional that allows for the description of the energies of the electron system. The second establishes that the electron density can be obtained from a one-electron theory.

In this chapter, we give an overview of DFT, presenting the essential characteristics of the theory.

2.1 Overview

We begin by considering the Hamiltonian[1] for a non-relativistic Coulomb system of N electrons and M fixed nuclei using the Born–Oppenheimer approximation [11]:

$$\hat{H} = -\frac{1}{2}\sum_{i=1}^{N}\nabla_i^2 - \sum_{i=1}^{N}\sum_{I=1}^{M}\frac{Z_I}{|\mathbf{r}_i - \mathbf{R}_I|} + \sum_{i=1}^{N}\sum_{j>i}^{N}\frac{1}{|\mathbf{r}_i - \mathbf{r}_j|}, \tag{2.1}$$

In the equation above, the electrons are represented by the lower case and the nuclei by the upper case, $\mathbf{R}_I$ and $\mathbf{r}_i$ are the position vectors of nuclei and electrons, respectively, and Z_I is the atomic number of nucleus I.

The total electronic energy is the expectation value of the Hamiltonian:

$$E = \left\langle \hat{T} \right\rangle + \int \mathrm{d}^3 r\, v_{\text{ext}}(\mathbf{r}) n(\mathbf{r}) + \left\langle \hat{V}_{int} \right\rangle, \tag{2.2}$$

$\hat{T}$ represents the kinetic energy operator of the electrons, $\hat{V}_{int}$ the electron-electron interaction and $v_{\text{ext}}(\mathbf{r})$ the external potential due to the nuclei.

---

[1] Atomic units are used.

Although the Hamiltonian depends only on the spatial coordinates of the electron, to fully describe the electronic system, it is necessary to consider the spins. We do this by making the wavefunction depend on both the spatial coordinates and the spins of the electrons. Each electron is described by three spatial coordinates and one spin coordinate, collectively represented by $\mathbf{x} = (\mathbf{r}, \sigma)$. Thus, the wavefunction of the N-electron system is represented by $\Psi(\mathbf{x}_1, \mathbf{x}_2, ..., \mathbf{x}_N)$. Additionally, the wavefunction has to obey the spin-statistics theorem[12], which states that the wavefunction for many electrons must be antisymmetric to the interchange of the coordinate $\mathbf{x}$ of any two electrons (both space and spin):

$$\Psi(\mathbf{x}_1, ..., \mathbf{x}_i, ..., \mathbf{x}_j, ..., \mathbf{x}_N) = -\Psi(\mathbf{x}_1, ..., \mathbf{x}_j, ..., \mathbf{x}_i, ..., \mathbf{x}_N). \tag{2.3}$$

The probability density of finding an electron with spin σ_1 at the position $\mathbf{r}_1$ in the volume $\mathrm{d}^3 r_1$, an electron with spin σ_2 at $\mathbf{r}_2$ in the volume $\mathrm{d}^3 r_2$, ..., and an electron with spin σ_N at $\mathbf{r}_N$ in the volume $\mathrm{d}^3 r_N$ is $N! \left|\Psi\left(\mathbf{r}_1\sigma_1, \ldots, \mathbf{r}_N\sigma_N\right)\right|^2 \ \mathrm{d}^3 r_1 \ldots \mathrm{d}^3 r_N$ [13] if the wavefunctions are normalised such that:

$$\sum_\sigma \int \mathrm{d}^3 r \left|\Psi(\mathbf{r}, \sigma)\right|^2 = \langle \Psi | \Psi \rangle = 1. \tag{2.4}$$

The electron spin density, $n(\mathbf{r}, \sigma)$, is defined so that $n(\mathbf{r}, \sigma)\ \mathrm{d}^3 r$ is the probability of finding an electron with spin σ in a volume element $\mathrm{d}^3 r$ at $\mathbf{r}$. It is found integrating over the $\mathbf{x}_i$ coordinates of the (N-1) remaining electrons:

$$\begin{aligned} n(\mathbf{r}, \sigma) &= \frac{1}{(N-1)!} \sum_{\sigma_2 \ldots \sigma_N} \int \mathrm{d}^3 r_2 \ldots \int \mathrm{d}^3 r_N N! \left|\Psi\left(\mathbf{r}\sigma, \mathbf{r}_2\sigma_2, \ldots, \mathbf{r}_N\sigma_N\right)\right|^2 \\ &= N \sum_{\sigma_2 \ldots \sigma_N} \int \mathrm{d}^3 r_2 \ldots \int \mathrm{d}^3 r_N \left|\Psi\left(\mathbf{r}\sigma, \mathbf{r}_2\sigma_2, \ldots, \mathbf{r}_N\sigma_N\right)\right|^2. \end{aligned} \tag{2.5}$$

The former equations, (2.4) and (2.5), guarantee that:

$$\sum_\sigma \int \mathrm{d}^3 r \, n(\mathbf{r}, \sigma) = N. \tag{2.6}$$

2.2 The Hohenberg and Kohn Theorems

In 1964, Hohenberg and Kohn (HK) proved, for the non-relativistic case and non-degenerate ground-state, that the ground state density $n_0(\mathbf{r})$ uniquely determines the external potential except for a constant. Generalisations of the theory to include degenerate states, spin polarisation, and time dependence were made later, but only a description of the original work will be presented here. Hohenberg and Kohn's results can be summarised in the subsequent two theorems:

- **Theorem 1:** *The external potential is uniquely determined, apart from an additive constant, by the ground state particle density* $n_0(\mathbf{r})$*;*
- **Theorem 2:** *The exact ground state energy is the global minimum of the energy functional,* $E\left[n\right]$*, and the density that minimises it is the ground state density.*

The first theorem is proved through *reductio ad absurdum.* Let $\{v_{\text{ext}}\}$ be the set of all v_{ext} that differ by more than a constant, $\{\Psi\}$ the set of the non-degenerate ground-state wavefunctions, and $\{n(\mathbf{r})\}$ the set of possible ground-state densities such that:

$$\{v_{\text{ext}}\} \overset{\text{A}}{\longmapsto} \{\Psi\} \overset{\text{B}}{\longmapsto} \{n\} \tag{2.7}$$

The first HK theorem is equivalent to stating that the map $A \circ B$ is injective. The mapping B, between the space of wavefunctions and the set of possible densities, is injective by the definition of density (2.5). To prove that two different potentials generate different ground-state densities, first, we must prove that the mapping A is also injective.

We suppose that two different external potentials, $v_{\text{ext}}^{(1)}$ and $v_{\text{ext}}^{(2)}$, give the same ground-state wavefunction Ψ. From the Schrödinger equation follows that:

$$\left(\hat{T} + \hat{V}_{int} + v_{\text{ext}}^{(1)}\right)|\Psi\rangle = E^{(1)}|\Psi\rangle\,, \tag{2.8}$$

$$\left(\hat{T} + \hat{V}_{int} + v_{\text{ext}}^{(2)}\right)|\Psi\rangle = E^{(2)}|\Psi\rangle\,. \tag{2.9}$$

Subtracting equations (2.8) and (2.9),

$$\left(v_{\text{ext}}^{(1)} - v_{\text{ext}}^{(2)}\right)|\Psi\rangle = \left(E^{(1)} - E^{(2)}\right)|\Psi\rangle\,, \tag{2.10}$$

we obtain an equality that contradicts our initial assumption that $v_{\text{ext}}^{(1)}$ and $v_{\text{ext}}^{(2)}$ differ by more than a constant. Thus, we prove that mapping A is injective.

We suppose that two different external potentials, $v_{\text{ext}}^{(1)}$ and $v_{\text{ext}}^{(2)}$, give the same ground-state density $n(\mathbf{r})$. Each potential leads to distinct Hamiltonians, $\hat{H}^{(1)}$ and $\hat{H}^{(2)}$, leading to two different wavefunctions, $\Psi^{(1)}$ and $\Psi^{(2)}$. $\Psi^{(1)}$ is the ground state associated with $\hat{H}^{(1)}$, and $\Psi^{(2)}$ is associated with $\hat{H}^{(2)}$. Using the variational principle, for two non-degenerate states follows that:

$$E^{(1)} = \left\langle \Psi^{(1)} \middle| \hat{H}^{(1)} \middle| \Psi^{(1)} \right\rangle < \left\langle \Psi^{(2)} \middle| \hat{H}^{(1)} \middle| \Psi^{(2)} \right\rangle. \tag{2.11}$$

We can rewrite the right-hand side of the equation as:

$$\begin{aligned}\left\langle\Psi^{(2)}\middle|\,\hat{H}^{(1)}\,\middle|\Psi^{(2)}\right\rangle &= \left\langle\Psi^{(2)}\middle|\,\hat{H}^{(2)}\,\middle|\Psi^{(2)}\right\rangle + \left\langle\Psi^{(2)}\middle|\,\hat{H}^{(1)} - \hat{H}^{(2)}\,\middle|\Psi^{(2)}\right\rangle \\ &= E^{(2)} + \int \mathrm{d}^3r \left[v_{\text{ext}}^{(1)}(\mathbf{r}) - v_{\text{ext}}^{(2)}(\mathbf{r})\right] n_0(\mathbf{r}).\end{aligned} \tag{2.12}$$

Then, substituting this result on equation (2.11), we obtain:

$$E^{(1)} < E^{(2)} + \int \mathrm{d}^3r \left[v_{\text{ext}}^{(1)}(\mathbf{r}) - v_{\text{ext}}^{(2)}(\mathbf{r})\right] n_0(\mathbf{r}). \tag{2.13}$$

In the same way, if we had interchanged the superscripts (1) and (2) of equations (2.11) and (2.12), we would arrive at:

$$E^{(2)} < E^{(1)} + \int \mathrm{d}^3r \left[v_{\text{ext}}^{(2)}(\mathbf{r}) - v_{\text{ext}}^{(1)}(\mathbf{r})\right] n_0(\mathbf{r}). \tag{2.14}$$

Summing equations (2.13) and (2.14), we reach a contradictory inequality:

$$E^{(1)} + E^{(2)} < E^{(1)} + E^{(2)}. \tag{2.15}$$

Thus, we prove that two different potentials that differ by more than one constant cannot originate the same ground-state density.

The HK's theorem establishes a relation between the external potential, v_{ext}, and the ground-state density $n_0(\mathbf{r})$. In turn, v_{ext} determines the many-body wavefunction Ψ of all system states (both ground state and excited) since it fully defines the Hamiltonian in the Schrödinger equation. By definition of the density, if the ground-state wavefunction Ψ_0 is known, the ground-state density is also known. Accordingly, v_{ext}, Ψ_0 and $n_0(\mathbf{r})$ determine each other uniquely, and the many-body wavefunction Ψ is a functional of the ground-state density.

As a consequence of the HK's theorem, any observable can be written as a functional of the density since:

$$O[n] = \langle\Psi[n]|\hat{O}|\Psi[n]\rangle\,, \tag{2.16}$$

including the total energy:

$$E\,[n] = T\,[n] + V_{int}\,[n] + \int \mathrm{d}^3r\, v_{\text{ext}}(\mathbf{r}) n(\mathbf{r}). \tag{2.17}$$

We can define a universal functional[2], $F\left[n\right]$, valid for any number of electrons on any external potential, composed by the kinetic and potential energy of the interacting electron system:

$$F\left[n\right] = T\left[n\right] + V_{int}\left[n\right]. \tag{2.18}$$

The original HK proof is restricted to ground-state densities that can be generated by some external potential. Such densities are called "V-representable". The "V-representable" densities define a space of possible densities within which we can construct density functionals. The ground-state energy assumes its minimum at the correct ground-state density if the possible densities are restricted to the ones that follow the condition:

$$N = \int \mathrm{d}^3r\, n(\mathbf{r}). \tag{2.19}$$

The constraint of fixed N can be handled by introducing a Lagrange multiplier μ:

$$\begin{aligned}
&\frac{\delta}{\delta n}\left(E[n] - \mu \int \mathrm{d}^3r\, n(\mathbf{r})\right) = 0 \Leftrightarrow \\
\Leftrightarrow &\frac{\delta}{\delta n}\left(F[n] + \int \mathrm{d}^3r\, v_{\mathrm{ext}}(\mathbf{r})n(\mathbf{r}) - \mu \int \mathrm{d}^3r\, n(\mathbf{r})\right) = 0 \Leftrightarrow \\
\Leftrightarrow &\frac{\delta F[n]}{\delta n} + v_{\mathrm{ext}}(\mathbf{r}) - \mu = 0.
\end{aligned} \tag{2.20}$$

2.3 The Kohn-Sham System

The electronic Hamiltonian can only be solved exactly for very simple systems such as hydrogen-like atoms with just one electron. From the theory of Hohenberg and Kohn, Kohn and Sham proposed using an auxiliary non-interacting electron system to treat the interacting electron system. The objective is to determine the original system's solution by numerically solving the Schrödinger equation for an auxiliary system.[10]

We start by considering an N-independent electron system constructed in such a way that its ground-state density is the same as that of the interacting one we are interested in. The auxiliary system is governed by the one-particle Schrödinger equation:

$$\left[-\frac{1}{2}\nabla^2 + v_s(\mathbf{r})\right]\psi_i(\mathbf{r}) = \epsilon_i\psi_i(\mathbf{r}), \tag{2.21}$$

where v_{s} is the external potential in which the non-interacting particles move, and ϕ_i are the independent one-particle Kohn-Sham orbitals. The ground-state wavefunction can be written as a Slater determinant of the Kohn-Sham orbitals that are the eigenstates of the

---

[2] The universal functional varies for different particles, depending on their masses and interactions.

lowest energy solutions of the Schrödinger equation. Additionally, the system's density is:

$$n(\mathbf{r}) = \sum_{i=1}^{N} \theta\left(\mu - \varepsilon_i\right) \left|\psi_i(\mathbf{r})\right|^2, \tag{2.22}$$

in equation above μ is the chemical potential chosen to guarantee condition (2.19). The Heaviside step function ensures that the orbitals with energies below μ are singly occupied and above it empty.

For the non-interacting system, the electron-electron interaction vanishes. Therefore, the total energy functional can be written as:

$$E_s[n] = T_s[n] + \int \mathrm{d}^3r \, v_{\mathrm{s}}(\mathbf{r}) n(\mathbf{r}), \tag{2.23}$$

in which T_s is the non-interacting energy.

By minimising the total energy while maintaining constant the number of particles as for the interacting system (equation 2.20), we obtain:

$$\begin{aligned} &\frac{\delta}{\delta n}\left(T_s[n] + \int \mathrm{d}^3r \, v_{\mathrm{s}}(\mathbf{r}) n(\mathbf{r}) - \mu_s \int \mathrm{d}^3r \, n(\mathbf{r})\right) = 0 \Leftrightarrow \\ \Leftrightarrow &\frac{\delta T_s[n]}{\delta n} + v_{\mathrm{s}}(\mathbf{r}) - \mu_s = 0 \end{aligned} \tag{2.24}$$

Concerning the real system, the Kohn-Sham approach starts by re-arranging the energy's functional terms in the following way:

$$\begin{aligned} &E[n] = (T[n] - T_{\mathrm{s}}[n]) + (V_{int}[n] - U[n]) + T_s[n] + U[n] + \int \mathrm{d}^3r \, v_{\mathrm{ext}}(\mathbf{r}) n(\mathbf{r}) \Leftrightarrow \\ \Leftrightarrow &E[n] = T_{\mathrm{s}}[n] + U[n] + E_{\mathrm{xc}}[n] + \int \mathrm{d}^3r \, v_{\mathrm{ext}}(\mathbf{r}) n(\mathbf{r}), \end{aligned} \tag{2.25}$$

where $U[n]$ denotes the Hartree electrostatic self-repulsion of the electron density $n(\mathbf{r})$:

$$U[n] = \frac{1}{2} \int \mathrm{d}^3r \int \mathrm{d}^3r' \frac{n(\mathbf{r}) n\left(\mathbf{r}'\right)}{\left|\mathbf{r} - \mathbf{r}'\right|}. \tag{2.26}$$

From equation (2.25), we notice that the difference between the kinetic and internal energies of the proper system and the Hartree and kinetic energy of the auxiliary one are grouped together, defining a new functional, the exchange and correlation energy:

$$E_{\mathrm{xc}}[n] = T\left[n\right] - T_{\mathrm{s}}\left[n\right] + V_{int}\left[n\right] - U[n] \tag{2.27}$$

The minimisation of the energy for the original interacting system now gives:

$$\begin{aligned}&\frac{\delta}{\delta n}\left(T_s[n]+U[n]+E_{\mathrm{xc}}[n]+\int \mathrm{d}^3r\, v_{\mathrm{ext}}(\mathbf{r})n(\mathbf{r})-\mu\int \mathrm{d}^3r\, n(\mathbf{r})\right)=0 \Leftrightarrow\\ &\Leftrightarrow \frac{\delta T_s[n]}{\delta n}+u[n](\mathbf{r})+v_{xc}[n](\mathbf{r})+v_{\mathrm{ext}}(\mathbf{r})-\mu=0\end{aligned} \tag{2.28}$$

where $u[n](\mathbf{r})$ represents the Hartree potential and $v_{xc}[n](\mathbf{r})$ the exchange-correlation potential. These potentials are defined as:

$$u[n](\mathbf{r})=\int \mathrm{d}^3r'\,\frac{n\left(\mathbf{r}'\right)}{\left|\mathbf{r}-\mathbf{r}'\right|}, \tag{2.29}$$

$$v_{xc}[n](\mathbf{r})=\frac{\delta E_{xc}[n]}{\delta n}. \tag{2.30}$$

The minimisation equations of both systems must be consistent, as they lead, by hypothesis, to the same density. Thus, substituting equation (2.24) in equation (2.28) yields:

$$v_s[n](\mathbf{r})=u[n](\mathbf{r})+v_{xc}[n](\mathbf{r})+v_{ext}(\mathbf{r})+\mu_s-\mu. \tag{2.31}$$

Any difference between the chemical potentials μ and μ_s can be absorbed into the external potential by the first HK theorem. Therefore, the Kohn-Sham potential $v_s(\mathbf{r})$ is given by:

$$v_s[n](\mathbf{r})=u[n](\mathbf{r})+v_{xc}[n](\mathbf{r})+v_{ext}(\mathbf{r}). \tag{2.32}$$

Substituting $v_s(\mathbf{r})$ in the Schrödinger equation of the auxiliary system, we obtain the Kohn-Sham equations:

$$\left[-\frac{1}{2}\nabla^2+v_s[n](\mathbf{r})\right]\psi_i(\mathbf{r})=\epsilon_i\psi_i(\mathbf{r}). \tag{2.33}$$

For a given $v_s(\mathbf{r})$, the Kohn-Sham equations have to be solved self-consistently assuming an initial density.[13]

If the precise form for $E_{xc}[n]$ was known, then the exact ground-state energy and density of the many-body electron problem could be found by solving the Kohn–Sham equations. However, only an approximate form of the exchange-correlation functional is attainable.[11] The following section is dedicated to it.

The potential $v_{ext}(\mathbf{r})$ corresponds to the Coulomb attraction between the nuclei and the electrons. However, when treated exactly, the Kohn-Sham equations become computationally expensive since the orthogonalisation of the valence orbitals makes the orbitals strongly oscillate near the core region, requiring an extensive basis set. Since the inner shell electrons are tightly bound to the nucleus, they do not participate actively in chemical binding, forming an almost inert core with the nucleus. Therefore, we can replace the Coulomb potential with an effective potential called pseudopotential, which is essentially a Coulomb potential screened by the core electrons. The pseudopotential is weaker than the Coulomb potential. By using it, we "remove" the core electrons from the problem, reducing the oscillations of the valence orbitals, thus making the calculations more efficient.[13]

2.4 Functionals for Exchange-Correlation

The exchange-correlation energy defined previously by equation (2.27) results from the decrease in the probability of finding an electron in the vicinity of another one due to the Pauli exclusion principle and the repulsive Coulomb interaction.

The Hohenberg and Kohn formulation (section 2.2) shows that the addition of the kinetic and the internal energy functionals corresponds to an unknown universal functional (equation 2.18). Therefore, as the exchange and correlation functional depends upon it, we must find an approximate form.

The success of DFT comes from the fact that it has been proven to be possible to find remarkably successful approximations for the exchange-correlation energy functional.

Different exchange-correlation functional approximations have been organised in five rungs of increasing complexity and accuracy on the "Jacob's ladder"[14] (Fig. 2.1). Each rung is also more computationally demanding, being the choice dependent on various aspects, namely the precision and time balance desired.

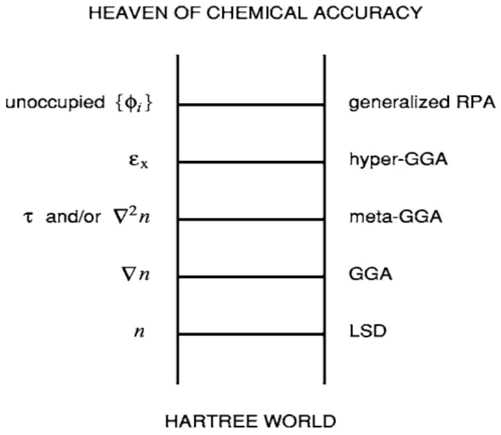

Fig. 2.1 Jacobs' ladder of density functional approximations for the exchange and correlation energy functionals.[15]

1. **Local spin-density approximation (LSDA):** The first rung on the ladder corresponds to the simplest spin-density approximation for the exchange-correlation energy, a local functional of the density. It is a functional of the spin-up and spin-down electronic

densities and is defined as the following:

$$E_{\mathrm{xc}}^{\mathrm{LSDA}}\left[n_{\uparrow}, n_{\downarrow}\right]=\int \mathrm{d}^{3} r n(\mathbf{r}) \varepsilon_{\mathrm{xc}}^{\mathrm{unif}}\left(n_{\uparrow}(\mathbf{r}), n_{\downarrow}(\mathbf{r})\right). \tag{2.34}$$

Here, $\varepsilon_{\mathrm{xc}}^{\mathrm{unif}}$ denotes the exchange-correlation energy per particle of an electron gas with uniform spin densities. The energy density at each point is assumed to be the same as in an uniform electron gas with a density equal to the density at that point in space.

LSDA is exact in the limit of uniform spin density. Due to the more reasonable resemblance with the homogenous electron gas, LSDA is more accurate for solids than atoms and molecules.

2. **Generalised gradient approximation (GGA):** As an improvement over LSDA, various GGAs were developed. GGA was motivated by the second-order gradient expansion, valid for slow varying densities. The correction yields exchange-correlation energy that is a functional of both the density and its gradient:

$$E_{\mathrm{xc}}^{\mathrm{GGA}}\left[n_{\uparrow}, n_{\downarrow}\right]=\int \mathrm{d}^{3} r n(\mathbf{r}) \varepsilon_{\mathrm{xc}}^{\mathrm{GGA}}\left(n_{\uparrow}(\mathbf{r}), n_{\downarrow}(\mathbf{r}), \nabla n_{\uparrow}(\mathbf{r}), \nabla n_{\downarrow}(\mathbf{r})\right). \tag{2.35}$$

The generalised gradient approximations include the widely used non-empirical functional of Perdew, Burke, and Ernzerhof (PBE) in condensed matter physics.

3. **Meta generalised gradient approximation (Meta-GGA):** As the laplacian appears in the fourth-order gradient expansion, it would be the subsequent logical correction to the exchange-correlation energy. However, the KS kinetic orbital energy densities are also functionals of the density and allow the satisfaction of more constraints:

$$\tau_{\sigma}=\frac{1}{2} \sum_{i=1}^{N} \theta\left(\mu-\varepsilon_{i \sigma}\right)\left|\nabla \psi_{i \sigma}\right|^{2}. \tag{2.36}$$

Therefore, we define the Meta-GGA approximation as:

$$E_{\mathrm{xc}}^{\mathrm{MGGA}}\left[n_{\uparrow}, n_{\downarrow}\right]=\int \mathrm{d}^{3} r n(\mathbf{r}) \varepsilon_{\mathrm{xc}}^{\mathrm{MGGA}}\left(n_{\uparrow}(\mathbf{r}), n_{\downarrow}(\mathbf{r}), \nabla n_{\uparrow}(\mathbf{r}), \nabla n_{\downarrow}(\mathbf{r}), \tau_{\uparrow}, \tau_{\downarrow}\right). \tag{2.37}$$

Meta-GGAs are semi-local functionals of both the density and occupied KS orbitals. The higher rungs are non-local functionals of the orbitals.

4. **Hyper generalised gradient approximation (Hyper-GGA):** On the hyper-GGA rung, the exact exchange energy density is considered. We define the Hyper-GGA

approximation as:

$$E_{\mathrm{xc}}^{\mathrm{HGGA}}\left[n_{\uparrow}, n_{\downarrow}\right] = \int \mathrm{d}^3 r\, n(\mathbf{r}) \varepsilon_{\mathrm{xc}}^{\mathrm{HGGA}}\left(n_{\uparrow}(\mathbf{r}), n_{\downarrow}(\mathbf{r}), \nabla n_{\uparrow}(\mathbf{r}), \nabla n_{\downarrow}(\mathbf{r}), \tau_{\uparrow}, \tau_{\downarrow}, \varepsilon_{\mathrm{x}\uparrow}, \varepsilon_{\mathrm{x}\downarrow}\right). \tag{2.38}$$

All the Kohn-Sham orbitals are included on the fifth rung, both occupied and unoccupied.[15]

Chapter 3

Topological insulators

Condensed matter physics uses models to understand the properties of states of matter. One of the areas of interest involves developing models to study phase transitions. The standard approach to classifying states of matter is based on spontaneously broken symmetries. However, some states could not be understood in terms of symmetry breaking, leading to a new model of classification based on the concept of topological order. The first of which was the quantum Hall state. Some of its fundamental properties remain constant under smooth changes in material parameters and cannot change unless a quantum phase transition occurs.[1]

The realisation that spin-orbit coupling can lead to topological insulating phases renewed interest in understanding the role of topology in classifying phases of matter.

Like the integer quantum Hall state, topological insulators have gapless edge states protected by time-reversal symmetry and can be understood in the topology and band theory framework.

This chapter will briefly present how topology is used in condensed matter physics, introduce key concepts like topological invariants, explain the integer quantum Hall effect, and finally, characterise topological insulators.

3.1 Topology

Topology is a branch of mathematics that studies geometrical objects' properties that are preserved under continuous transformations.

The role of topology is most easily depicted by considering two-dimensional surfaces in three dimensions. The most common example is given thinking of a sphere and a doughnut. A doughnut can be smoothly deformed into a mug or ring. However, a doughnut cannot be continuously deformed into a sphere. Both objects are distinguished by an integer topological invariant named genus, g, which counts the number of holes, as shown by figures 3.2(c) and

3.2(f). Surfaces with different genus numbers are said to be topologically distinct, while the others are topologically equivalent.

We can use the Gauss-Bonnet theorem for surfaces to determine an object's topological invariant. The theorem states that the integral of the Gaussian curvature, K, over a closed surface S defines an integer topological invariant called the Euler characteristic, χ:

$$\chi = \frac{1}{2\pi} \int_S K \, dA. \tag{3.1}$$

The Euler characteristic is related to the genus by $\chi = 2 - 2g$.[16]

3.2 Bloch's theorem

Bloch's theorem states that the eigenstates $\psi_{n\mathbf{k}}$ of the one-electron Hamiltonian $\hat{H} = -\frac{1}{2}\nabla^2 + U(\mathbf{r})$, in a periodic potential, $U(\mathbf{r}+\mathbf{R}) = U(\mathbf{r})$, can be written as the product of a plane wave by a function with the Bravais lattice periodicity:

$$\psi_{n\mathbf{k}}(\mathbf{r}) = e^{i\mathbf{k}\cdot\mathbf{r}} u_{n\mathbf{k}}(\mathbf{r}), \tag{3.2}$$

where

$$u_{n\mathbf{k}}(\mathbf{r}) = u_{n\mathbf{k}}(\mathbf{r}+\mathbf{R}), \tag{3.3}$$

for any lattice vector $\mathbf{R} = l_1\mathbf{a}_1 + l_2\mathbf{a}_2 + l_3\mathbf{a}_3$, $l = (l_1, l_2, l_3)$ are integers and $\mathbf{a}_1$, $\mathbf{a}_2$ and $\mathbf{a}_3$ are the primitive lattice vectors.[17]

Substituting the Bloch wave function $\psi_{n\mathbf{k}}$ in the time-independent Schrödinger equation, we obtain:

$$H \left|\psi_{n\mathbf{k}}\right\rangle = E_{n\mathbf{k}} \left|\psi_{n\mathbf{k}}\right\rangle. \tag{3.4}$$

The wave vector $\mathbf{k}$ is the crystal momentum, and n denotes the "band index", counting states of the same $\mathbf{k}$ in terms of increasing energy. Eigenvalues $E_{n\mathbf{k}}$ with the same n define an energy band, and the set of energy bands forms the band structure.

The space of unique crystal momentum $\mathbf{k}$ is the Brillouin zone. Regarding topology, the BZ can be considered a unit circle in 1D, a 2-torus in 2D and a 3-torus in 3D.[18]

Equations (3.2) and (3.3) imply that the Bloch functions obey the condition:

$$\psi_{n\mathbf{k}}(\mathbf{r}+\mathbf{R}) = e^{i\mathbf{k}\cdot\mathbf{R}} \psi_{n\mathbf{k}}(\mathbf{r}). \tag{3.5}$$

For the following purposes, working with cell-periodic Bloch functions is more convenient than with the Bloch wave functions as, unlike the Bloch wave functions, the cell-periodic Bloch function and its derivatives are all defined in a single primitive unit cell of the crystal.

The cell-periodic Bloch functions are defined as:

$$u_{n\mathbf{k}}(\mathbf{r}) = e^{-i\mathbf{k}\cdot\mathbf{r}}\psi_{n\mathbf{k}}(\mathbf{r}). \tag{3.6}$$

It is also common to define a k-dependent Bloch Hamiltonian whose eigenfunctions are the cell-periodic Bloch functions:

$$H(\mathbf{k}) = e^{-i\mathbf{k}\cdot\mathbf{r}}He^{i\mathbf{k}\cdot\mathbf{r}}. \tag{3.7}$$

3.3 Berry phases and Berry Curvature

The Berry phase is a phase angle describing a global phase accumulation of a complex vector as it is carried around on a closed loop in a complex vector space. It varies from 0 to 2π.

In the context of crystalline solids, the vectors are the Bloch states, and the complex vector space is the Brillouin zone. We consider a path parameterized by the wavevector components k_j in the Brillouin zone. The Berry phase associated with the band n takes the form:

$$\phi_n = \oint \mathbf{A}_n(\mathbf{k}) \cdot d\mathbf{k}, \tag{3.8}$$

where $\mathbf{A}_n(\mathbf{k})$ is defined as the Berry connection:

$$\mathbf{A}_n(\mathbf{k}) = i\left\langle u_{n\mathbf{k}} \middle| \boldsymbol{\nabla}_k \middle| u_{n\mathbf{k}} \right\rangle. \tag{3.9}$$

The cell-periodic Bloch's states are smooth and differentiable functions of $\mathbf{k}$. Under a gauge transformation, the Bloch functions are transformed as:

$$\left|\tilde{u}_{n\mathbf{k}}\right\rangle = e^{i\beta_n(\mathbf{k})}\left|u_{n\mathbf{k}}\right\rangle, \tag{3.10}$$

with $\beta_n(\mathbf{k})$ being some real periodic function in reciprocal space. It can be shown that the Berry connection is not gauge invariant. However, the Berry phase is a gauge invariant modulo of 2π,

$$\tilde{\phi}_n = \phi_n + 2\pi m, \quad m \in \mathbb{Z}, \tag{3.11}$$

meaning that around a closed loop, $\left|u_{n\mathbf{k}}\right\rangle$ acquires a well-defined Berry phase.

The Berry curvature is the curl of the Berry connection:

$$\Omega_{n,\mu\nu}(\mathbf{k}) = \partial_\mu A_{n\nu}(\mathbf{k}) - \partial_\nu A_{n\mu}(\mathbf{k}). \tag{3.12}$$

In 3D, the Berry curvature can be expressed in the pseudovector notation, acquiring the more familiar form: $\boldsymbol{\Omega}_n(\mathbf{k}) = \boldsymbol{\nabla} \times \mathbf{A}_n$. The Berry curvature is gauge invariant.

Once defined as the curl of the Berry connection, we can apply Stoke's theorem to associate the Berry flux Φ_S through a surface S to the Berry phase ϕ_P around its boundary P. In the 3D parameter space, it reads:

$$\Phi_S = \int_S \Omega(\mathbf{k}) \cdot \hat{\mathbf{n}}\, dS = \oint \mathbf{A}(\mathbf{k}) \cdot d\mathbf{k} = \phi_P. \tag{3.13}$$

The term "connection" is taken from differential geometry. A close analogy between the Berry connection and the Berry curvature can also be made with electromagnetism. The Berry connection is analogous to the vector potential and the Berry curvature to a magnetic field.[18]

3.4 Classical Hall effect

We consider a metallic system in an applied electrical and magnetic field. Using the Drude model, the equation of motion of an electron in this system is:

$$\frac{d\mathbf{p}}{dt} = -e\left(\mathbf{E} + \mathbf{v} \times \mathbf{B}\right) - \frac{\mathbf{p}}{\tau}, \tag{3.14}$$

where τ is the scattering time.

In the steady state, $\frac{d\mathbf{p}}{dt} = 0$, and using $\mathbf{p} = m\mathbf{v}$, the previous equation takes the form:

$$\mathbf{E} = -\mathbf{v} \times \mathbf{B} - \frac{m\mathbf{v}}{e\tau}, \tag{3.15}$$

or, in terms of the current density $\mathbf{j} = -ne\mathbf{v}$, where n is the density of electron in the metal,

$$\mathbf{E} = \frac{\mathbf{j} \times \mathbf{B}}{ne} + \frac{m}{ne^2\tau}\mathbf{j}. \tag{3.16}$$

Now we consider a thin metallic plate in a uniform magnetic field $\mathbf{B} = B\hat{e}_z$. When an electric field is applied in the x-direction, a current density j_x flows in the x-direction. The Lorentz force, $\mathbf{F} = ev_xB\hat{e}_y$, causes charge accumulation along a lateral plate edge, inducing an electric field in the y-direction. This electric field produces a voltage in the y-direction, the Hall voltage, V_H.

A relation between the electrical field and the current vector applies in the tensor form:

$$\mathbf{E} = \boldsymbol{\rho}\mathbf{j}, \tag{3.17}$$

$$\begin{pmatrix} E_x \\ E_y \end{pmatrix} = \begin{pmatrix} \rho_{xx} & \rho_{xy} \\ \rho_{yx} & \rho_{yy} \end{pmatrix} \begin{pmatrix} j_x \\ j_y \end{pmatrix} \tag{3.18}$$

where $\boldsymbol{\rho}$ is the resistivity tensor.

The components of the resistivity tensor are obtained from (3.14):

$$\rho_{xx} = \rho_{yy} = \frac{m}{ne^2\tau}, \tag{3.19}$$

$$\rho_{xy} = -\rho_{yx} = \frac{B}{ne}. \tag{3.20}$$

The Hall resistance is defined as

$$R_H = \frac{E_y}{j_x B} = \frac{\rho_{yx}}{B}. \tag{3.21}$$

The conductivity tensor is defined as the inverse of the resistivity tensor:

$$\boldsymbol{\sigma} = \begin{pmatrix} \sigma_{xx} & \sigma_{xy} \\ \sigma_{yx} & \sigma_{yy} \end{pmatrix} = \boldsymbol{\rho}^{-1}. \tag{3.22}$$

where

$$\sigma_{xx} = \frac{\rho_{xx}}{\rho_{xx}^2 + \rho_{yy}^2}, \tag{3.23}$$

$$\sigma_{yy} = \frac{\rho_{yy}}{\rho_{xx}^2 + \rho_{yy}^2}, \tag{3.24}$$

and

$$\sigma_{xy} = -\sigma_{yx} = -\frac{\rho_{xy}}{\rho_{xx}^2 + \rho_{xy}^2}. \tag{3.25}$$

3.5 Integer quantum Hall effect and the Chern number

The integer quantum Hall effect was discovered in 1980 by von Klitzing, Dorda and Pepper.[19] It occurs when an electron gas restricted to two dimensions at a low temperature ($< 4\,\mathrm{K}$) is subjected to a perpendicular strong magnetic field. In these conditions, they have shown that the Hall resistivity[1] is constant over a range of magnetic field B, forming plateau (Fig. 3.1). On plateau, the Hall resistivity takes quantised values:

$$\rho_{xy} = \frac{2\pi\hbar}{e^2}\frac{1}{\mu}, \quad \mu \in \mathbb{Z}, \tag{3.26}$$

where μ is an integer value measured with remarkable precision of 1 part in 10^9.

---

[1] Experimentally, we measure the resistance, which is related to the resistivity by the dimensions of the sample. However, in 2D, the transverse resistance $R_{xy} = \frac{V_y}{I_x} = \frac{E_y L_y}{J_x L_y} = -\rho_{xy}$ and the Hall resistivity ρ_{xy} coincide and do not depend on the sample's dimensions.

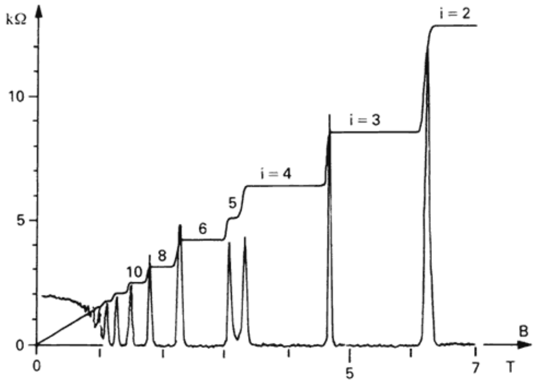

Fig. 3.1 The Hall resistivity ρ_{xy} takes on a plateau form over a range of magnetic field values B.

In addition, on the plateau, the longitudinal resistivity vanishes $\rho_{xx} = 0$. It peaks only when ρ_{xy} jumps to the next plateau. Thus, the Hall conductivity is just the inverse of the Hall resistivity:

$$\sigma_{xy} = \frac{e^2}{2\pi\hbar}\mu, \quad \mu \in \mathbb{Z}. \tag{3.27}$$

The Hamiltonian for one electron in a 2D system subjected to a perpendicular magnetic field $\mathbf{B} = B\hat{e}_z$ is:

$$H = \frac{1}{2m}(\mathbf{p} + e\mathbf{A})^2, \tag{3.28}$$

where $\mathbf{A}$ is the magnetic vector potential defined so that its curl is equal to the magnetic field, $\boldsymbol{\nabla} \times \mathbf{A} = \mathbf{B}$, and $\mathbf{p} = m\dot{\mathbf{x}} - e\mathbf{A}$ is the canonical momentum.

Since $\mathbf{B} = B\hat{e}_z$, we can choose, in the Landau gauge,, the vector potential:

$$\mathbf{A} = Bx\hat{e}_y. \tag{3.29}$$

Accordingly, the Hamiltonian becomes translationally invariant in the y-direction, commuting with the momentum operator p_y:

$$H = \frac{1}{2m}\left(p_x^2 + (p_y + eBx)^2\right). \tag{3.30}$$

If we restrict to the subspace of momentum $p_y = \hbar k$, we obtain the Schrödinger equation of an 1D harmonic oscillator centered at $x = -kl_B$:

$$\left[\frac{1}{2m}p_x^2 + \frac{m\omega_c^2}{2}\left(x + kl_B^2\right)^2\right]\Psi_k = E_{n,k}\Psi_k, \tag{3.31}$$

where $\omega_c = \frac{eB}{m}$ is the cyclotron frequency and $l_B = \sqrt{\frac{\hbar}{eB}}$ is the system's magnetic length.

The eigenvalues obtained by solving the equation above are designated by Landau levels and are given by:

$$E_n = \hbar\omega_c\left(n + \frac{1}{2}\right), \quad n \in \mathbb{N}. \tag{3.32}$$

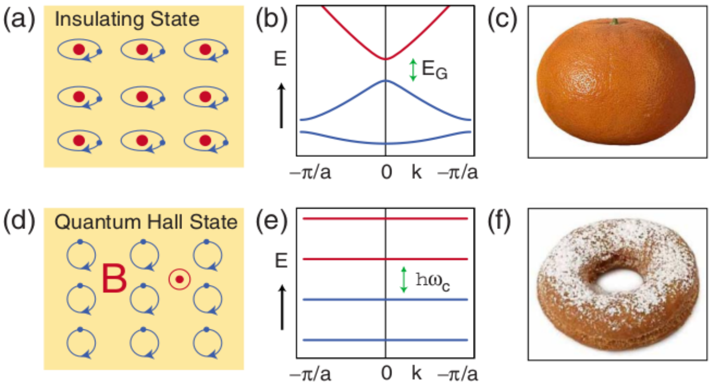

Fig. 3.2 Representation of states of matter. (a)–(c) The insulating state. (d)–(f) The quantum Hall state. (a) An atomic insulator. (b) A simple model insulating band structure. (c) The sphere is a surface with genus $g = 0$. (d) The cyclotron motion of electrons. (e) The Landau levels. (f) The doughnut is a surface with genus $g = 1$. The Chern number C that distinguishes the two states is a topological invariant similar to the genus.[1]

Now, we consider a rectangular sample with dimensions $L_x \times L_y$. The eigenfunctions of the system are the product of a plane wave e^{iky} and the harmonic oscillator eigenfunctions. Then, the momentum in the y-direction can be quantised in multiples of $k = \frac{2\pi}{L_y}$. In the x-direction, x varies between $0 \leq x \leq L_x$ and is related to k by $x = -kl_B^2$. The wavefunctions are localized in the x-direction around $x = -kl_B^2$, so k is expected to vary between $-L_x/l_B^2 \leq k \leq 0$.

These last considerations also allow us to define the number of states per Landau level and the Landau levels' filling factor μ. The number of states per energy level is defined as:

$$N = \frac{L_y}{2\pi}\int_{-L_x/l_B^2}^{0} dk = \frac{L_xL_y}{2\pi l_B^2} = \frac{eAB}{2\pi\hbar} = \frac{\Phi}{\Phi_0}, \tag{3.33}$$

where $A = L_xL_y$ is the sample area, Φ_0 is a flux quantum, and Φ is the total flux through the sample. The number of states is thus the number of flux quantum throughout the sample. The filling factor $\mu = \frac{n_e 2\pi\hbar}{eB}$ is the electronic density n_e divided by the number of electrons per unit area.

If η Landau levels are filled below the Fermi Energy (E_F), and the levels above E_F are empty, there is an energy gap separating the occupied and the empty energy levels. In the presence of a periodic potential, the Landau levels disperse with k, leading to a band structure that looks like the one of an ordinary insulator. If η is between two Landau levels, the density of states looks like the one of a metal.

Two quantum systems described by gapped band structures are topologically equivalent if the system's Bloch Hamiltonian $H(\mathbf{k})$ can be continuously deformed into each other without closing the energy gap at any point along the connecting path. Topologically equivalent systems are thus classified considering the equivalence of classes of $H(\mathbf{k})$. These classes are distinguished by the Chern number, a topological invariant.

Although the quantum Hall state and the ordinary insulator have a gapped bandstructure, the ordinary insulator and the quantum Hall effect are characterised by different Chern numbers.[20]

The Chern theorem states that the Berry flux is just 2π times the Chern number for any closed surface. Thus, in the 2D Brillouin zone, the Chern number of the band n is the total Berry flux in the Brillouin zone:

$$C_n = \frac{1}{2\pi} \int dk^2 \mathbf{\Omega}_n. \tag{3.34}$$

The total Chern number is a sum over all occupied bands, and it remains invariant even in the presence of degeneracy between occupied bands:

$$C = \sum_{n=1}^{N} C_n, \quad C \in \mathbb{Z}. \tag{3.35}$$

Considering the Hall system defined on a torus, Thouless, Kohmoto, Nightingale, and den Nijs[21] (TKNN) showed that using the Kubo formula for the Hall conductivity yields the form of the equation (3.27), with μ being identical to the total Chern number, C. Since the Chern number is always an integer, the Hall conductivity cannot change continuously. It is, therefore, invariant under a smooth variation of the Hamiltonian.

Alongside topology, edge states observed in the sample boundary play an essential role in the electronic transport quantisation in the quantum Hall effect.

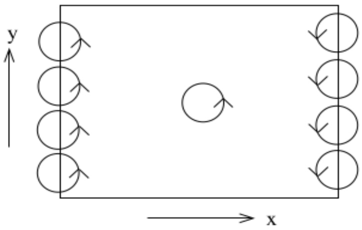

Fig. 3.3 Charged particles move along circular orbits. At the edge, the particles collide and bounce back, generating edge currents.

Charged particles move along circular orbits in the same direction in the presence of a magnetic field. Therefore, the electrons' orbits must collide and bounce off near the sample's edge, as shown in figure 3.3. Thus electrons execute a skipping motion, moving in only one direction along the edge. Since the electrons propagate in only one direction, these particles are chiral. They move in one direction on one side of the sample and in the opposite direction on the other side. Inside the sample, electrons are localised. They do not carry current nor contribute to conductivity. Therefore, no states are available for backscattering, so the edge states are insensitive to disorder.[20]

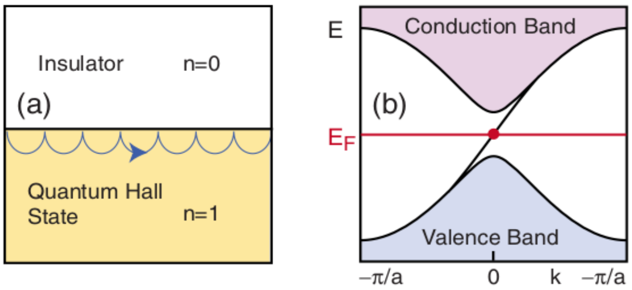

Fig. 3.4 The interface between a quantum Hall state and an insulator has chiral edge mode. (a) The skipping cyclotron orbits. (b) A single edge state connects the valence band to the conduction band.[1]

The edge states are closely related to the bulk topology, a feature of the bulk-boundary correspondence. Figure 3.4 shows the boundary between a quantum Hall state (C=1) and a standard insulator (C=0). Regarding topology, the Chern number has to change in the interface between the two states. This change implies that the energy gap vanishes. Therefore, there will have to be edge states that intersect the Fermi level.

3.6 Time Reversal symmetry

Unlike other symmetries, time reversal (TR) symmetry is represented by an antiunitary operator.[2]

The time reversal operator can be written as the product $\Theta = UK$ of a unitary operator U by a complex conjugation operator K. For particles with spin 1/2, it is frequently represented by:

$$\Theta = e^{i\pi S_y/\hbar}K, \tag{3.36}$$

where S_y is a spin operator and K is a complex conjugation operator. In this case, $\Theta^2 = -1$.

---

[2] An operator is said to be antiunitary if it preserves the norm of a vector and is antilinear. Transforming the states $|\alpha\rangle$ and $|\beta\rangle$ as: $|\alpha\rangle \longrightarrow |\tilde{\alpha}\rangle = \Theta|\alpha\rangle$, $|\beta\rangle \longrightarrow \left|\tilde{\beta}\right\rangle = \Theta|\beta\rangle$, the operator has to obey the following: $\left\langle\tilde{\beta}\middle|\tilde{\alpha}\right\rangle = \langle\beta|\alpha\rangle^*$ and $\Theta(c_1|\tilde{\alpha}\rangle + c_2\left|\tilde{\beta}\right\rangle) = c_1^*\Theta|\alpha\rangle + c_2^*\Theta|\beta\rangle$.

A consequence of TR symmetry is Kramers' theorem, which states that all energy eigenvalues of a time invariant Hamiltonian are at least twofold (doubly) degenerate. TR symmetry implies that the Bloch Hamiltonian must satisfy the following:

$$\Theta H(\mathbf{k})\Theta^{-1} = H(-\mathbf{k}). \tag{3.37}$$

When spin-orbit interactions are negligible, Kramers' theorem causes degeneracy between spin-up and spin-down energy levels. On the other hand, if spin-orbit interactions are present, it lifts Kramer's degeneracy everywhere in the Brillouin zone, except at particular points at which $\mathbf{k} = -\mathbf{k}$. These special k-points where the bands are degenerate are known as time-reversal invariant momentum (TRIM).[16]

3.7 $\mathbb{Z}_2$ insulators

2D ferromagnetic insulators that break time-reversal symmetry when an external magnetic field is applied, like quantum Hall states, can be classified according to their Chern number. However, in the framework of the bulk-boundary correspondence, an additional topological class of insulating states is possible. Nonmagnetic insulators that do not break time-reversal symmetry and belong to the trivial class C=0 allow a new insulating phase due to intrinsic spin-orbit interaction. Similarly to the Chern number, a new topological invariant ν characterises this class.

3.7.1 Two-dimensional topological insulator: Quantum spin Hall insulator

A quantum Hall state was first described to exist in graphene by Haldane's model.[22] The electron's spin is ignored in this model. However, a new topological phase was theorised by introducing a spin term in the previous model, the Quantum spin Hall insulator.[23]

Since intrinsic spin-orbit interaction commutes with the spin operator S_z, we can treat spin-up and spin-down states independently. Separately, the Hamiltonians for the spin-up and spin-down electrons violate time-reversal symmetry, predicting a Hall conductivity. However, when considered together, time-reversal symmetry is not broken because it reverses $\mathbf{p}$, interchanging spin-up and spin-down Hamiltonians, and converts the identities of spin-up and spin-down electrons.[18]

We suppose two copies of the quantum hall state are considered and an electric field is applied. Then, two Hall currents with opposing signs appear. The currents cancel, and the sum of the total conductivity becomes zero. Nevertheless, a spin Hall current $\mathbf{J} = \frac{\hbar}{2e}(\mathbf{J}_\uparrow - \mathbf{J}_\downarrow)$ is generated. This current is characterised by a spin Hall conductivity $\sigma^s_{xy} = \frac{e}{2\pi}$.

Since a 2D topological insulator can be regarded as a copy of two quantum Hall states, it has gapless edge states. Although spin conservation is not a fundamental property, Kane and Mele[23] showed that edge states are protected due to time reversal even when spin conservation is violated. Moreover, Kramer's theorem guarantees that the states are degenerate at the $\mathbf{k} = 0$ crossing.

Let us consider the band structure of a 2D insulator whose Hamiltonian is time-invariant. In bulk, time reversal converts a spin-up state at $\mathbf{k}$ into a complex-conjugated spin-down one at $-\mathbf{k}$ with $E_{n\mathbf{k}} = E_{n,-\mathbf{k}}$, so we only have to consider half of the BZ. Depending on the system, edge states may exist inside the band gap. We can classify a system with edge states according to the $\mathbb{Z}_2$ invariant. If spin-orbit coupling (SOC) is strong, only the particular points $k_x = 0$ and $k_x = \pi/a$, designated by Γ_a and Γ_b, respectively, are doubly degenerate.

The edge states inside the energy gap can be connected to the valence and conduction bands in two ways, as shown by figure 3.5: The states cross the Fermi level an even number of times. In this case, the states can be eliminated by moving the Fermi energy slightly. If the states cross the Fermi level an odd number of times, they cannot be eliminated. The trivial insulator has an even number of Kramers pairs, being characterised by $\nu = 0$, while the 2D topological insulator has an odd number, being distinguished by $\nu = 1$.[16]

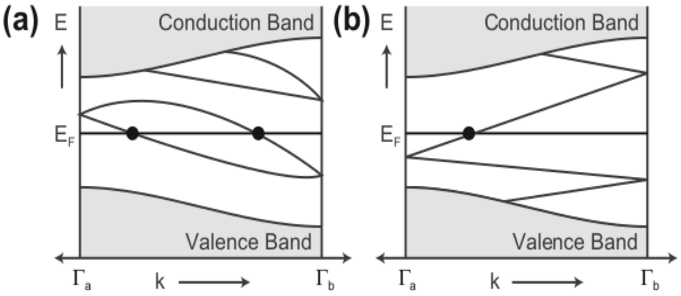

Fig. 3.5 Electronic dispersion between two Kramers degenerate points. In (a) the number of surface states crossing the Fermi energy E_F is even, whereas in (b) it is odd. An odd number of crossings leads to topologically protected metallic edge states.[1]

3.7.2 Determining the $\mathbb{Z}_2$ invariant

Since each band intersecting E_F at k_j has a Kramers pair of an edge state at $-k_j$, our objective is to relate the number of Kramers pairs with the $\mathbb{Z}_2$ invariant across the interface.

One of the possible approaches to computing the $\mathbb{Z}_2$ invariant ν consists of defining an overlap unitary matrix:

$$w_{mn}(\mathbf{k}) = \langle u_m(\mathbf{k})|\Theta|u_n(-\mathbf{k})\rangle \,, \tag{3.38}$$

where $|u_n\rangle$ are the occupied Bloch states. The time-reversal symmetry implies that $w^{\intercal}(\mathbf{k}) = -w(-\mathbf{k})^3$ for 1/2 spin particles.

---

[3] $w^{\intercal}$ denotes the transpose of the matrix w.

In the 2D Brillouin zone, there are four TRIM points Γ_a such that $\mathbf{k} = -\mathbf{k}$. At these points the matrix w is antisymmetric.[4] For antisymmetric matrices, a number exists, the Pfaffian, whose square is equal to the matrix determinant:

$$Pf[w(\Lambda_a)] = \pm\det[w(\Lambda_a)]. \tag{3.39}$$

Since there is gauge freedom to define the Bloch states to be continuous everywhere in the BZ, we can define:

$$\delta_a = \frac{Pf[w(\Lambda_a)]}{\sqrt{\det[w(\Lambda_a)]}} = \pm 1. \tag{3.40}$$

By taking the product sign of δ_a over the four special points, we can determine the invariant ν:

$$(-1)^{\nu} = \prod_{a=1}^{4} \delta_a. \tag{3.41}$$

This approach can be extended to 3D topological insulators.[16]

3.7.3 Three-dimensional topological insulator

In 3D bulk, there are 8 TRIM points. The special k-points can be visualised as the vertices of a cube. The boundaries of a 3D crystal are 2D surfaces. The surface states that may exist can thus be labelled with the 2D crystal momentum $\mathbf{k}$. Due to TR, we only need to consider 1/8 of the BZ. Therefore, each wave vector k_j varies between 0 to π, as shown in figure 3.6. The 8 TRIM points form six time-invariant planes represented by shaded planes. As expected from the 2D $\mathbb{Z}_2$ classification, each plane is associated with an index ν_i. However, the indices are not independent. Four $\mathbb{Z}_2$ invariants characterise the 3D topological insulators $(\nu_0; \nu_1\nu_2\nu_3)$. The indices (ν_1, ν_2, ν_3) can be interpreted as the Miller indices used to specify directions and planes.[1]

---

[4] A matrix is antisymmetric if it satisfies the condition $A^{\intercal} = -A$. w is antisymmetric because $w^{\intercal}(\mathbf{k}) = -w(\mathbf{k})$.

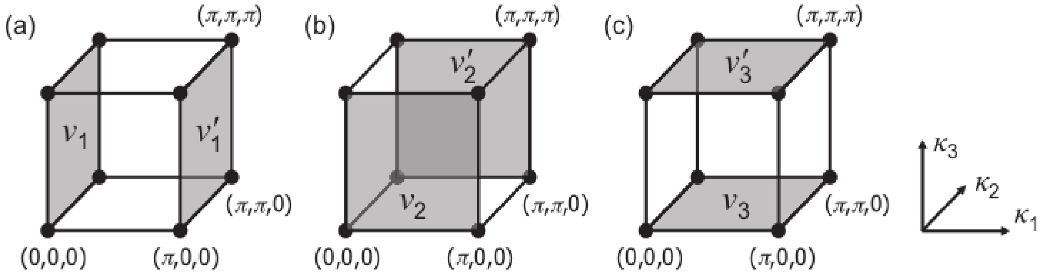

Fig. 3.6 View of the one-eighth of the BZ of a 3D TR-invariant insulator. The dots indicate TRIM; shaded planes indicate TR-invariant planes. Topological indices ν_1 and ν_1' are defined as the $\mathbb{Z}_2$ indices associated with the labeled TR-invariant planes in (a), and similarly for ν_2 and ν_2' in (b) and ν_3 and ν_3' in (c).[18]

A 3D time-reversal insulator is classified as strong if ν_0 is odd, weak if ν_0 is even, but at least one ν_j is odd and trivial if all indices are equal to zero $(0;000)$. The indices (ν_1, ν_2, ν_3) are equal to (ν_1', ν_2', ν_3') if the topological insulator (TI) is strong and equal to $(-\nu_1', -\nu_2', -\nu_3')$ if the topological insulator is weak.[18]

To describe the 3D topological insulators, we begin by considering the plane perpendicular to k_3. In the 2D reciprocal plane, four time-reversal invariant points must be degenerate, by the Kramers' theorem, so called Dirac points. As we move away from Dirac's points, SOC lifts the Kramers' degeneracy. Then, we can study how the Dirac points connect. In 3D, the surface states form a Fermi surface. In order to classify the topological insulators, we determine if the Fermi surface intersects the line that joins two TRIM points Λ_a and Λ_b an even or an odd number of times.

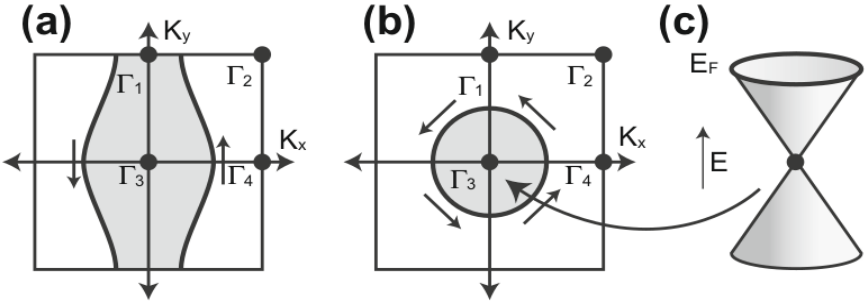

Fig. 3.7 Fermi circles in the surface Brillouin zone for (a) a weak topological insulator and (b) a strong topological insulator. (c) In the simplest strong topological insulator the Fermi circle encloses a single Dirac point.[16]

The simplest 3D topological insulator can be constructed by stacking 2D quantum spin Hall insulators. A possible Fermi surface that results from the stacking along the y-direction is represented in figure 3.7(a). In this case, one surface band intersects the path between Λ_3 and

Λ_4 one time, leading to a state called a weak topological insulator. Figure 3.7(b) represents the case of the simplest strong topological insulator. The Fermi surface encloses a Dirac point. The index ν_0 identifies a weak or strong TI by determining if Kramers' degenerate points are enclosed by a Fermi surface an even or an odd number of times, respectively.

On the one hand, time-reversal symmetry does not protect the weak topological insulator surface states since these states can be localised in the presence of disorder. On the other hand, in a strong topological insulator, the surface states are protected against disorder as long as the Hamiltonian is continuously deformed.

The surface of a 3D strong topological insulator has unique characteristics. It forms a 2D topological metal whose k-points are not spin degenerate. Since the states labeled with $\mathbf{k} = -\mathbf{k}$ must be degenerate, the spin must rotate with $\mathbf{k}$ around the Fermi surface as shown in figure 3.7(b).[1]

Chapter 4

Alloys Modelling

The use of electronic structure calculations for the design of novel materials for technological applications is becoming widespread. Alloys represent promising candidates due to the ability to model their structural and transport properties using different doping patterns. In this chapter, we give an insight into how to model random substitutional alloys computationally.

4.1 General Concepts

Alloys are solid mixtures of two or more chemical elements. Alloying generally refers to adding small amounts of elements to an element in greater concentration (the primary element) to improve its properties.[24] Typical examples are two copper alloys, bronze and brass. Bronze is composed primarily of copper, to which a small percentage of tin (12%) is added to increase its strength and hardness. Similarly, brass is constituted mainly of copper (66%), to which zinc is added instead of tin.

An ideal crystalline structure can be described by giving its lattice and a description of the arrangement of the atoms in a unit cell. The lattice is an infinite set of points given by integer sums of a set of linearly independent primitive lattice vectors. A unit cell is a region of the space that, when translated through all lattice vectors $\mathbf{R} = l_1\mathbf{a}_1 + l_2\mathbf{a}_2 + l_3\mathbf{a}_3$[1], fills all the space without overlapping. Moreover, the position of atoms in the unit cell is given by a basis relative to a lattice point. The numbers specifying the size of a unit cell are called lattice parameters.

Although alloys have approximately an underlying crystal lattice structure at the macroscopic scale, microscopically, there are fluctuations relative to an ideal lattice. For example, in a binary alloy composed of atoms A and B, atom A can bond to a various number of atoms of type A and B. Moreover, the distance between atoms A and B differs from the

---

[1] $l = (l_1, l_2, l_3)$ are integers and $\mathbf{a}_1$, $\mathbf{a}_2$ and $\mathbf{a}_3$ are the primitive lattice vectors, as defined in the previous chapter.

distance between atoms A and A, giving rise to multiple local motifs distributed throughout the sample.

Adding other elements corresponds to introducing impurities to the lattice structure of the primary elements.[25] Different concentrations of impurities lead to different structural and transport properties.

Depending on the atomic arrangement in the unit cell, the impurities can be classified as follow:

- substitutional: if an atom lattice site of a principal element is populated with an atom of a different atomic number Z;
- interstitial: if an atom occupies a position that does not belong to the crystal structure.

This classification extends to the alloys being usually classified as interstitial or substitutional.

When the elements are mixed to form a substitutional alloy, different possibilities can occur depending on the thermodynamics of the system (Fig. 4.1):

- They are not miscible, and segregation occurs, forming clusters;
- They form an ordered periodic structure;
- They form a random alloy.

We will focus on modelling random substitutional alloys.

Fig. 4.1 Possible mixing reactions of two elements in substitutional alloys.

4.2 Computational representation of random substitutional alloys

Random alloys are materials for which the alloys' stoichiometry gives the probability of finding an atom at a given lattice site.[25] However, not all atomic positions can be substituted. The empirical Hume-Rothery rules determine the chances of substitution of an atomic site. To obey these rules, the difference in atomic radii of two atoms must be less than 15%. Both atoms should crystallise in the same structure. The electronegativities should be similar, and the valences should be the same.

Computationally, crystalline materials can be represented by a unit cell with periodic boundary conditions, given that they have translation symmetry in all directions in bulk. Unlike ideal crystalline structures, the translation symmetry in the long-range order is absent in random substitutional alloys. However, these alloys can still be characterised by a distribution of many local chemical environments throughout the alloy, giving rise to polymorphous configurations.[26]

For a given lattice, different configurations correspond to symmetrically distinct atomic arrangements of the elements on the lattice. In other words, which atomic element is on each lattice site.

A derivative superstructure is a structure with the lattice vectors related to those of the "parent lattice" by a transformation matrix, $\mathbf{M}$, such that $\mathbf{A} = \mathbf{Ma}$. $\mathbf{a}$ is the matrix constructed from the basis vectors of the "parent lattice" row-wise, and $\mathbf{A}$ is the transformed supercell. If the determinant of $\mathbf{M}$ is an integer, then $\mathbf{A}$ is a derivative superstructure. For example, if the determinant of $\mathbf{M}$ is 1, a represents another basis for the same lattice. If the determinant of $\mathbf{M}$ equals 2, the derivative supercell is two times the volume of the initial cell.

To model alloys using electronic structure methods, one can consider all derivative supercell configurations of a "parent lattice" and impose artificial boundary conditions. The derivative superstructures configurations of a "parent lattice" can be generated using different codes, e.g. ATAT[27] and Enumlib[28]. In this work, the code Enumlib will be used.

The code Enumlib enumerates all the possible lattices and unique rotationally and translational atomic site occupations by the different elements of each lattice. The elimination of symmetrically equivalent configurations is done using group theory.[28]

As many supercells are needed to mimic the distribution of the local chemical environments, the process is computationally demanding. Different approaches that do not require the consideration of all derivative supercells have been developed.[29]

One approach to model alloys is using Virtual Crystal Approximation (VCA). It consists in studying a unit cell composed of fictitious atoms generated by averaging the pseudopotentials of the parent compounds.[30] Nevertheless, there are concerns with accuracy, especially for physical properties that are not linear, e.g. the energy gap.[29]

Another is the use of the Cluster expansion method, which is described in the next section.

4.3 Cluster expansion method

The cluster expansion method predicts any configuration's energy from the knowledge of a small number of configuration energies calculated from first principles calculations.[27]

Assuming the Born-Oppenheimer approximation and that the system is on the ground state, the energy can be written as a function of the nuclear coordinates $\{\mathbf{R}_I\}$ $(I = 1, ..., M$ atoms):

$$E = E(\mathbf{R}_1, ..., \mathbf{R}_M). \tag{4.1}$$

For random substitutional alloys, some atoms are substituted with atoms of another element on the same lattice positions. Therefore, it is reasonable to consider that the nuclear positions and lattice parameters of unit cells associated with an alloy's distinct configurations are fixed and are those of the "parent lattice".

As the positions are fixed, it is, in principle, possible to assign a number σ_I to each nuclear position on the lattice and use it to index the corresponding atomic number, Z. The energy function's variables are then reduced from $3M$ to M.

The set of numbers σ_I assigned to all lattice sites in the unit cell represents the arrangement of the atomic elements on the lattice - the configuration - and can be represented by a vector:

$$\boldsymbol{\sigma} = (\sigma_1, ..., \sigma_M). \tag{4.2}$$

In general, geometry optimisation does not affect the bijection between the lattice sites of the parent fixed lattice and the actual relaxed derivative structures. Thus, the energy can be written as a function of the occupations:

$$E \equiv E(\boldsymbol{\sigma}). \tag{4.3}$$

The cluster expansion is based on the Ising model for a magnetic system on a fixed lattice. Like the Ising model, cluster expansion is defined by assigning each lattice site of the parent lattice a spin-like variable, σ_I.

The method is described for the case of binary alloys, composed of two different elements, but it can be extended for multi-component alloys as described in [31]. For binary alloys, $\mathrm{A_{1-x}B_x}$, σ_I takes the value $+1$ or -1 depending on the atomic element occupying the site:

$$\sigma_I = \begin{cases} +1 & \text{if the site is occupied by atom A} \\ -1 & \text{if the site is occupied by atom B} \end{cases} \tag{4.4}$$

In order to determine a configuration's energy, a basis set to describe the interactions between lattice sites is needed. The basis is formed from clusters. A cluster α is a combination of lattice sites I, such as pairs or triplets, and is represented by $\alpha = (i, j, ...)$, depending on the number of sites forming it.

The energy per lattice site in terms of the basis of clusters is parameterised as follows:

$$E(\boldsymbol{\sigma}) = \sum_{\alpha} m_\alpha \bar{\Pi}_\alpha(\boldsymbol{\sigma}) J_\alpha. \tag{4.5}$$

The sum runs over all non-equivalent clusters by symmetry operations. The coefficient J_α denotes the "effective interaction strength", given in units of energy per atom and associated with the cluster α. The multiplicity m_α indicates the number of equivalent clusters by translational and rotational symmetries of the parent lattice. $\bar{\Pi}_\alpha(\boldsymbol{\sigma})$ is the correlation matrix. It is defined as an average over the spin products of the lattice sites normalised to the number of rotated/translated clusters on each site:

$$\bar{\Pi}_\alpha(\boldsymbol{\sigma}) = \frac{1}{N_\sigma m_\alpha} \sum_{\beta \equiv \alpha} \prod_{i \in \beta} \sigma_i. \tag{4.6}$$

Where N_σ represents the number of atomic sites in the configuration's unit cell, and $\prod_{i \in \beta} \sigma_i$ is the product over the spins of all lattice sites in the cluster β.[32]

The energy expansion given by equation (4.5) is, in principle, infinite as interactions up to M-body can be considered. However, generally, the energy converges rapidly for short-range interactions. Thus, the sum can be truncated to relevant clusters formed from close neighbour lattice sites.

The unknown coefficients J_α can then be determined by calculating the energies of a small number of the ordered alloy structures through ab-initio calculations. Finally, any alloy's configuration energy is predicted from the fit of the coefficients J_α to the energies of those ordered structures.

Once constructed, the cluster expansion allows modelling any alloy configuration's energy at a minimal computational cost since any configuration can be calculated without requiring first-principles calculation. A typical well-converged cluster expansion of the energy of an alloy necessitates calculating the energy of around 30 to 50 ordered structures.[27]

Other observables like the band gap require the first-principles calculation of more structures to be well-converged.

Chapter 5

Results and Discussion

5.1 Numerical details

This chapter presents the results of the DFT calculations done using Quantum ESPRESSO. Quantum ESPRESSO is a code used for electronic structure calculations and materials modelling based on DFT and plane-wave method.[7][8] The objective is to solve the Kohn-Sham equations for periodic systems.

As input for the band structure and density of states calculations, we need to provide the system's geometry, the cutoff energy, the k-point grid, the pseudopotential, and the exchange-correlation energy functional.

Convergence tests of the cutoff energy and the k-point grid have been made to guarantee that the geometry and the energy gap are accurately described. For all the compounds studied, we converged the total electronic energy as a function of the cutoff energy and the k-point grid. We have used a threshold of 5 meV/atom for the cutoff energy and 1 meV/atom for the k-point grid to select these values.

5.2 Bi_2Se_3 and Bi_2Te_3

Both bismuth selenide (Bi2Se3) and bismuth telluride (Bi2Te3) crystalise in a rhombohedral structure with five atoms per unit cell within the D_{3d}^5 (R$\bar{3}$m) space group. The systems can also be visualised as a hexagonal unit cell with a layered structure along the z-axis.[4] The crystal structure of Bi_2Se_3 is presented in figure 5.1. The rhombohedral unit cell vectors ($\mathbf{t}_{1,2,3}$) and the ones of the hexagonal cell ($\mathbf{a}_{1,2,3}$) are related by the following transformation:

$$\begin{pmatrix} \mathbf{t}_1 \\ \mathbf{t}_2 \\ \mathbf{t}_3 \end{pmatrix} = \begin{pmatrix} -1 & 0 & 1 \\ 1 & 0 & -1 \\ 1 & 1 & 1 \end{pmatrix} \begin{pmatrix} \mathbf{a}_1 \\ \mathbf{a}_2 \\ \mathbf{a}_3 \end{pmatrix} \tag{5.1}$$

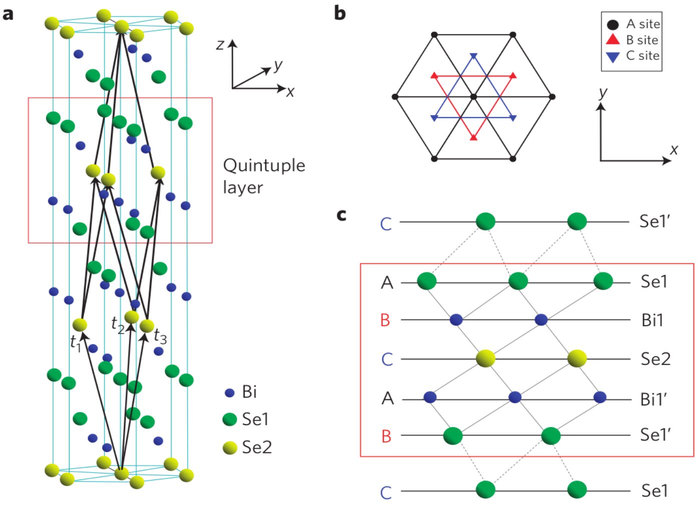

Fig. 5.1 Crystal structure of Bi_2Se_3.(a) Crystal structure of Bi_2Se_3 with three primitive lattice vectors denoted as $\mathbf{t}_{1,2,3}$. A quintuple layer with Se1–Bi1–Se2–Bi1'–Se1' is indicated by the red square. (b) Top view along the z-direction. The triangle lattice in one quintuple layer has three different positions, denoted as A, B and C. (c) Side view of the quintuple layer structure.[2]

The material consists of five atomic layers of bismuth (Bi) and selenium (Se) ordered as Se1–Bi1–Se2–Bi1'–Se1', forming a quintuple layer. The bond between quintuple layers is weak due to Van der Waals forces between selenium layers. Within the quintuple layer, the coupling is strong due to covalent bonds.

Van der Waals forces, which result from long-range interactions, are excluded from the Local Density Approximation (LDA) and Generalised Gradient Approximation (GGA) exchange-correlation energy functionals. However, some methods allow the incorporation of Van der Waals forces as a correction term to these functionals.[3]

Bi_2Se_3 and Bi_2Te_3 are materials whose topological features are allowed by time-reversal symmetry and spin-orbit coupling (SOC). Therefore, all the first-principles calculations were performed using SOC.

The compounds were considered in the rhombohedral structure with the initial geometry parameters taken from the experimental structure for Bi_2Se_3 and from the Materials Project[33] for Bi_2Te_3.

An example of the convergence tests made is shown in figures 5.2 and 5.3 for the Bi_2Se_3 calculation using LDA. From these figures, a cutoff energy of 85 Ry was chosen for the plane-wave set and a 10 × 10 × 10 k-point mesh for the Brillouin zone.

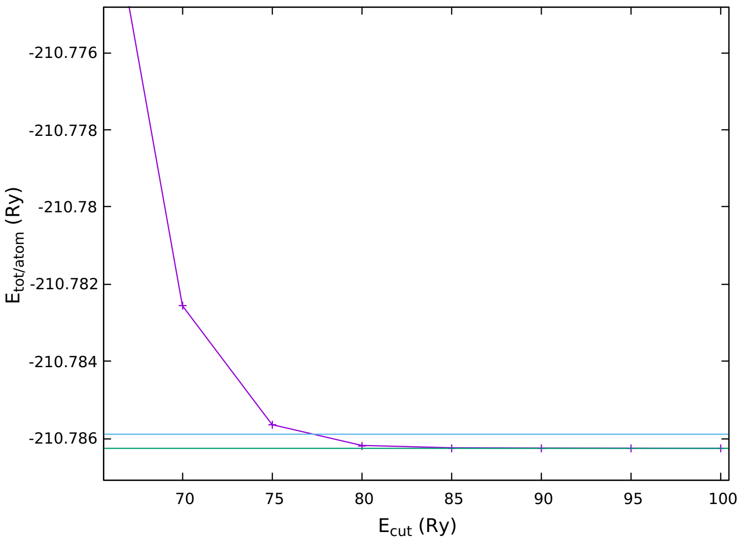

Fig. 5.2 Convergence of the total electronic energy as a function of the cutoff energy (E_{cut}) for Bi_2Se_3 using LDA.

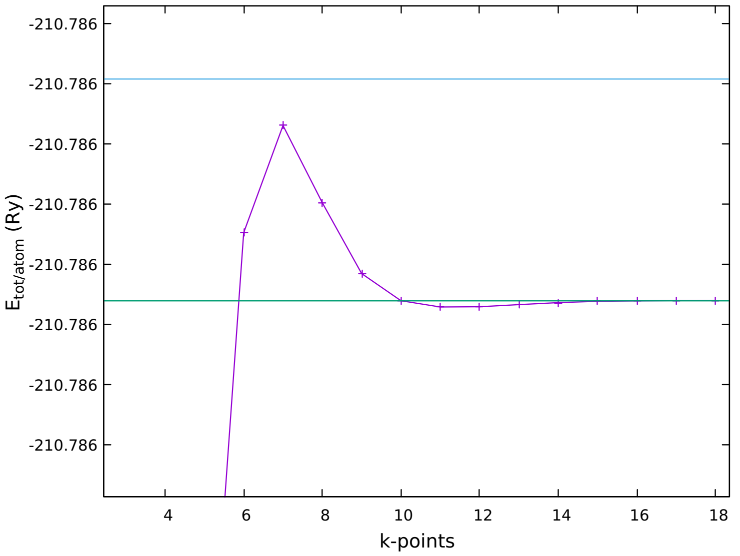

Fig. 5.3 Convergence of the total electronic energy as a function of the k-points for Bi_2Se_3 using LDA. The number of k-points shown in the x-axis is the M value in a $M \times M \times M$ k-point grid.

In order to choose an exchange-correlation energy functional that provides an accurate description of the band structure, the cell parameters and the energy gap, we have performed calculations using LDA and PBE with and without the D2 van der Waals corrections of Grimme et al.[6] and PBE_optb86b, that also includes van der Waals corrections.

Tables 5.1 and 5.2 show the optimised lattice parameters of the analysed compounds in terms of the hexagonal structure.

Table 5.1 Geometry optimized structural parameters for Bi_2Se_3 with and without van der Waals correction, using LDA, PBE and PBE_optB86B.

	Exp. [34]	LDA	LDA + VdW	PBE	PBE + VdW	PBE_optB86B
a (Å)	4.143	4.103	4.054	4.187	4.125	4.230
c (Å)	28.636	27.815	26.938	30.846	28.849	28.695

Table 5.2 Geometry optimized structural parameters for Bi_2Te_3 with and without van der Waals correction, using LDA, PBE and PBE_optB86B.

	Exp. [34]	LDA	LDA + VdW	PBE	PBE + VdW	PBE_optB86B
a (Å)	4.386	4.349	4.247	4.450	4.332	4.431
c (Å)	30.497	29.804	29.562	31.748	31.224	31.013

We observed that Van der Waals (VdW) correction is crucial in obtaining lattice parameters in good agreement with the experimental results, countering the under-binding of PBE. In the case of LDA, VdW corrections add to the over-binding of LDA, worsening it for both Bi_2Se_3 and Bi_2Te_3.

Using the optimised structures' lattice parameters that correspond to each exchange-correlation energy functional, we calculated the band structures along Γ-Z-F-Γ-L directions of the Brillouin zone. The band structures obtained are shown in figures 5.4 to 5.7 for Bi_2Se_3 and 5.9 to 5.12 for Bi_2Te_3. Additionally, we have determined a band structure using PBE with LDA geometry to understand the sensitivity of the band structure to the lattice parameters. All the band structures are compared to that obtained with LDA with Van der Waals correction since it was the functional selected for subsequent calculations. $\Gamma = (0, 0, 0)$, $L = (0.5, 0, 0)$, $F = (0.5, 0.5, 0)$ and $Z = (0.5, 0.5, 0.5)$ correspond to the four nonequivalent time-reversal invariant points.[2] The coordinates of the symmetry k-points are given in fractions of the reciprocal lattice vectors as defined by Setyawan and Curtarolo.[35]

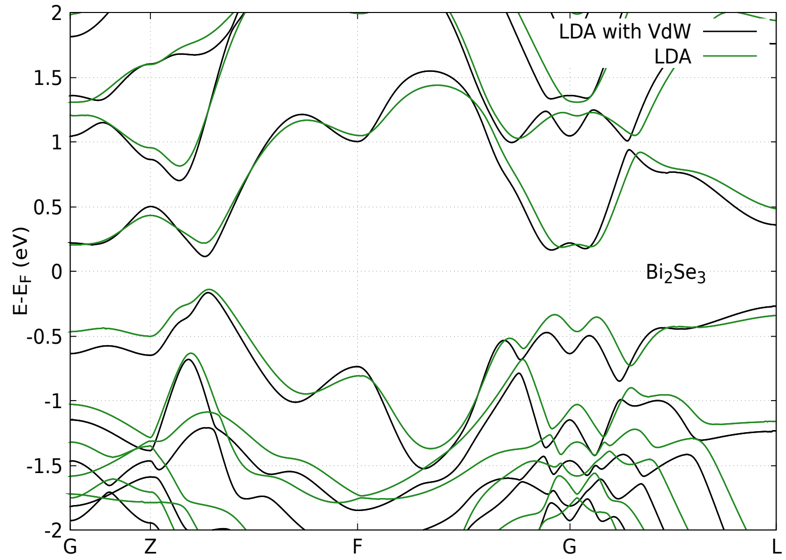

Fig. 5.4 Band structure for Bi_2Se_3 with spin-orbit coupling using LDA with van der Waals correction with the structure obtained from geometry optimisation using LDA with vdW correction, and LDA with the structure obtained from geometry optimisation using LDA. We set the Fermi energy level at zero, as determined by Quantum ESPRESSO.

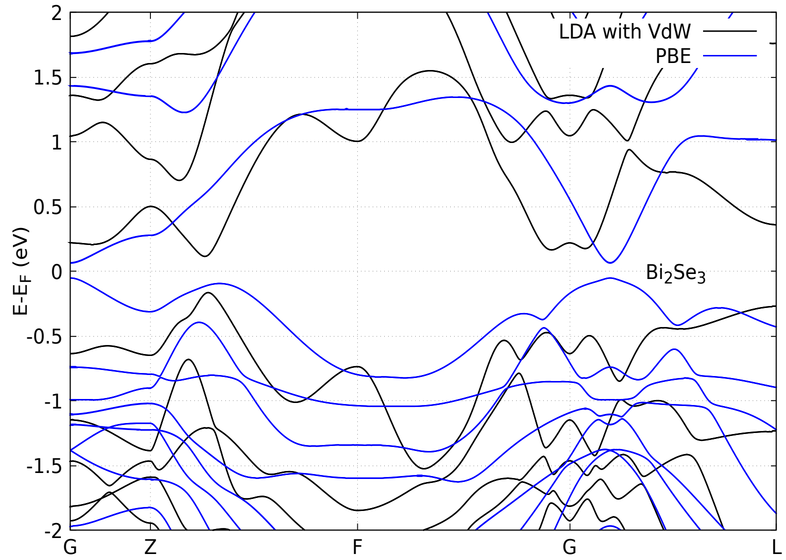

Fig. 5.5 Band structure for Bi_2Se_3 with spin-orbit coupling using LDA with van der Waals correction with the structure obtained from geometry optimisation using LDA with vdW correction, and PBE with the structure obtained from geometry optimisation using PBE. We set the Fermi energy level at zero, as determined by Quantum ESPRESSO.

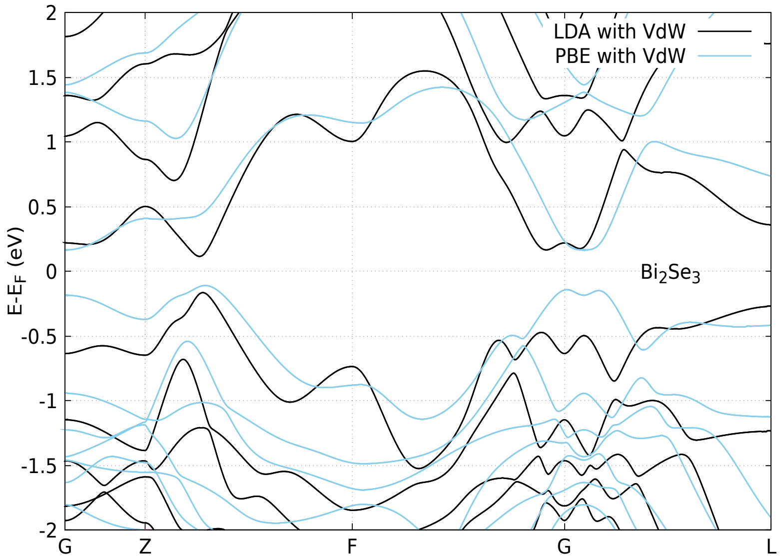

Fig. 5.6 Band structure for Bi$_2$Se$_3$ with spin-orbit coupling using LDA with van der Waals correction with the structure obtained from geometry optimisation using LDA with vdW correction, and PBE with vdW correction with the structure obtained from geometry optimisation using PBE with vdW correction. We set the Fermi energy level at zero, as determined by Quantum ESPRESSO.

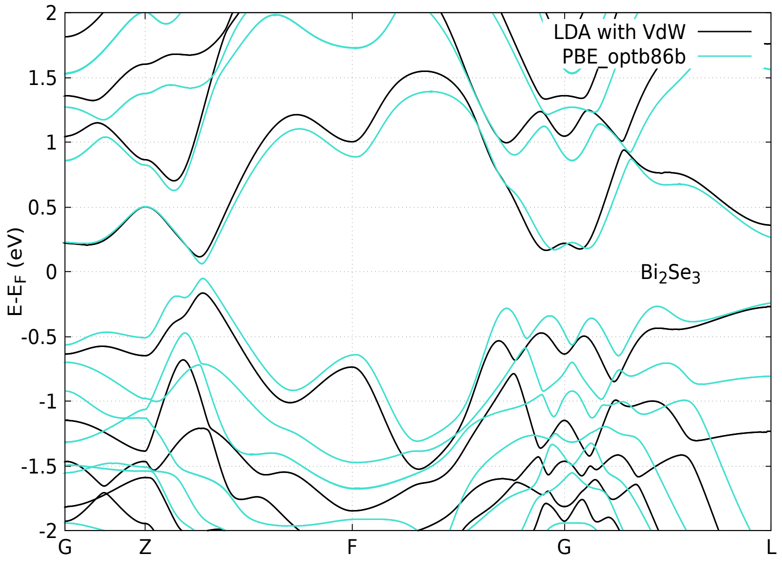

Fig. 5.7 Band structure for Bi$_2$Se$_3$ with spin-orbit coupling using LDA with van der Waals correction with the structure obtained from geometry optimisation using LDA with vdW correction, and PBE_optB86B with the structure obtained from geometry optimisation using PBE_optB86B. We set the Fermi energy level at zero, as determined by Quantum ESPRESSO.

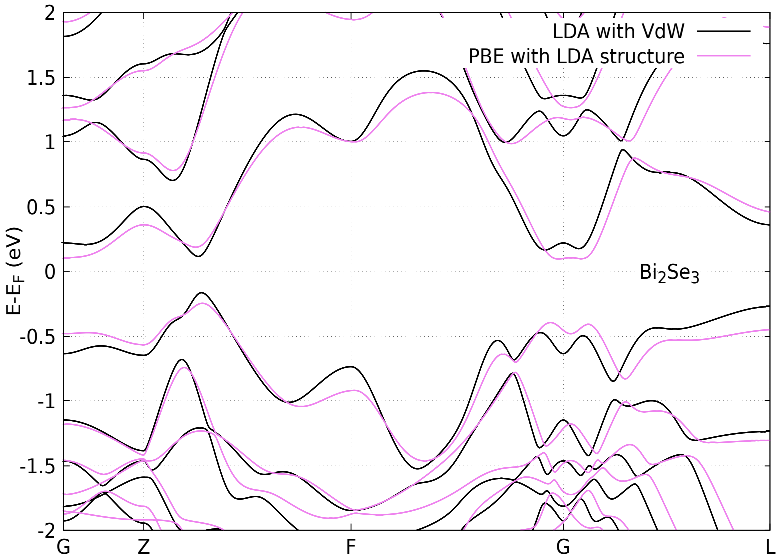

Fig. 5.8 Band structure for Bi_2Se_3 with spin-orbit coupling using LDA with van der Waals correction with the structure obtained from geometry optimisation using LDA with vdW correction, and PBE with the structure obtained from geometry optimisation using LDA. We set the Fermi energy level at zero, as determined by Quantum ESPRESSO.

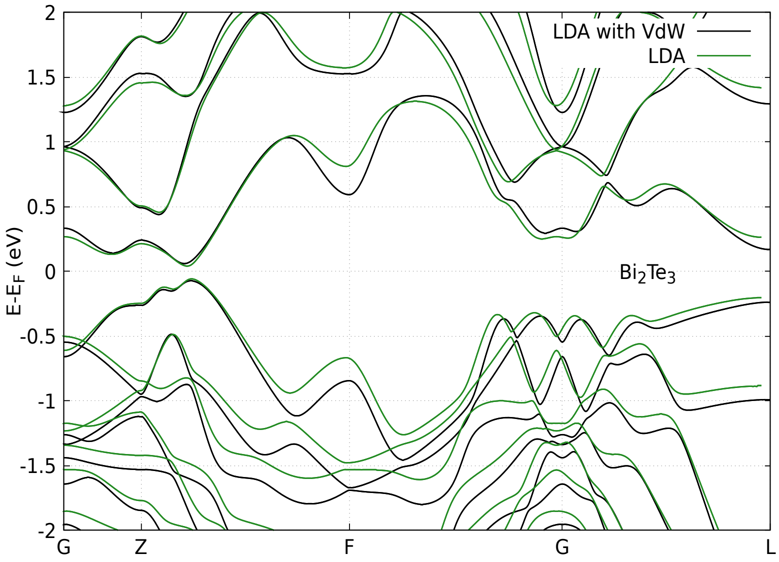

Fig. 5.9 Band structure for Bi_2Te_3 with spin-orbit coupling using LDA with van der Waals correction with the structure obtained from geometry optimisation using LDA with vdW correction, and LDA with the structure obtained from geometry optimisation using LDA. We set the Fermi energy level at zero, as determined by Quantum ESPRESSO.

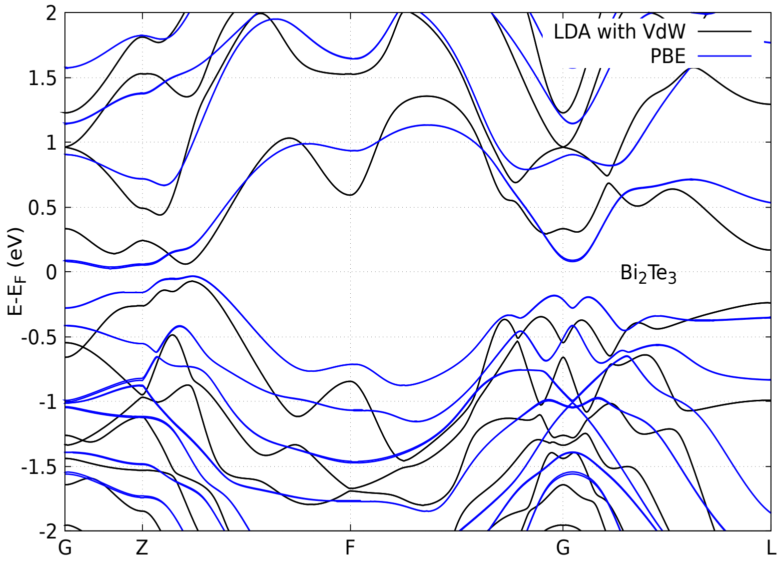

Fig. 5.10 Band structure for Bi_2Te_3 with spin-orbit coupling using LDA with van der Waals correction with the structure obtained from geometry optimisation using LDA with vdW correction, and PBE with the structure obtained from geometry optimisation using PBE. We set the Fermi energy level at zero, as determined by Quantum ESPRESSO.

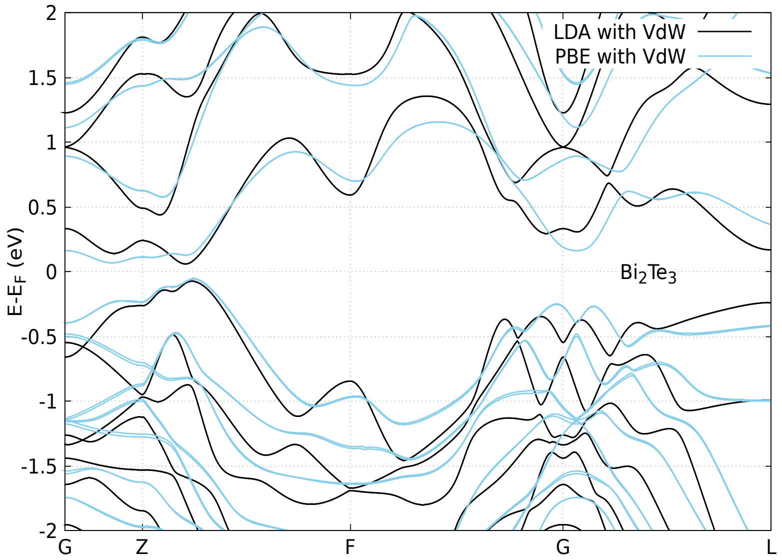

Fig. 5.11 Band structure for Bi_2Te_3 with spin-orbit coupling using LDA with van der Waals correction with the structure obtained from geometry optimisation using LDA with vdW correction, and PBE with vdW correction with the structure obtained from geometry optimisation using PBE with vdW correction. We set the Fermi energy level at zero, as determined by Quantum ESPRESSO.

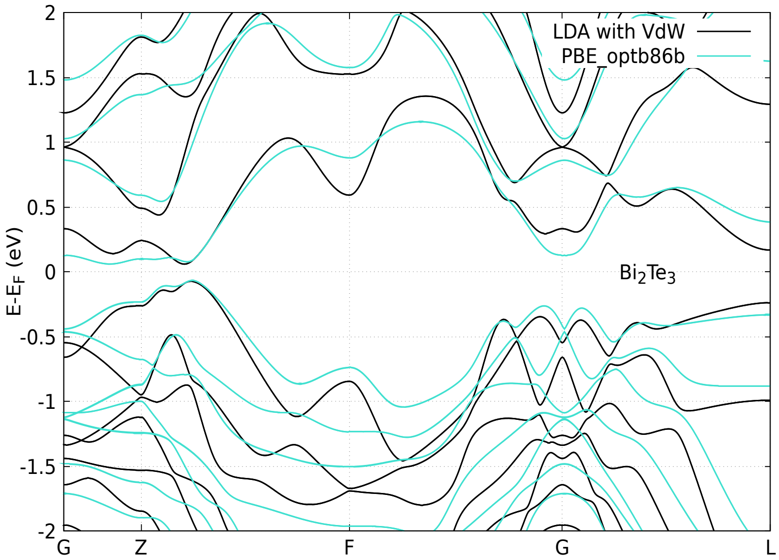

Fig. 5.12 Band structure for Bi_2Te_3 with spin-orbit coupling using LDA with van der Waals correction with the structure obtained from geometry optimisation using LDA with vdW correction, and PBE_optB86B with the structure obtained from geometry optimisation using PBE_optB86B. We set the Fermi energy level at zero, as determined by Quantum ESPRESSO.

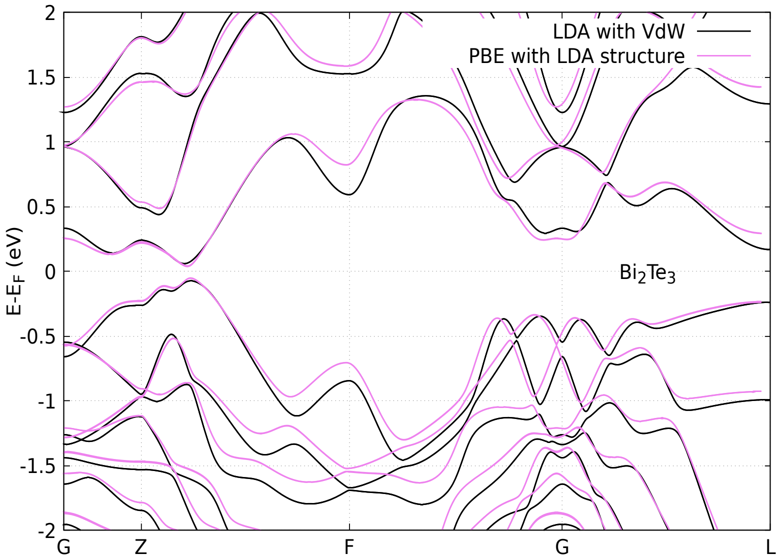

Fig. 5.13 Band structure for Bi_2Te_3 with spin-orbit coupling using LDA with van der Waals correction with the structure obtained from geometry optimisation using LDA with vdW correction, and PBE with the structure obtained from geometry optimisation using LDA. We set the Fermi energy level at zero, as determined by Quantum ESPRESSO.

Around point Γ in the band structure, there is an inversion between the conduction band and the valence band. The band inversion is a feature of the bulk-edge correspondence, a characteristic of $\mathbb{Z}_2$ topological insulators. This feature is visible in all band structures except the one determined with PBE for Bi_2Se_3. However, the band inversion is present using PBE with LDA geometry and PBE with Van der Waals corrections, indicating that the change of lattice parameters has a significant influence on the band structure.

From the band structures, we have determined the energy gaps as the difference between the minimum of the conduction band and the maximum of the valence band. The results are reported in table 5.3.

Although PBE with Van der Waals corrections lattice parameters are in better agreement with experiments, the band structure and the energy gap are better predicted using LDA with Van der Waals correction. Henceforward, we will use LDA with van der Waals correction as the exchange-correlation energy functional in alloys calculations.

Table 5.3 Energy band gap for Bi_2Se_3 and Bi_2Te_3 with and without van der Waals correction, using LDA, PBE and PBE_optB86B.

		Exp.[36][37]	LDA	LDA +VdW	PBE	PBE +VdW	PBE_optB86B
Bi_2Se_3	E_{gap} (eV)	0.2–0.3	0.325	0.279	0.115	0.275	0.113
Bi_2Te_3	E_{gap} (eV)	0.15	0.099	0.133	0.058	0.127	0.127

5.3 $\mathbf{Bi_2Se_{3-x}Te_x}$

Enumlib code (section 4.2) was used to determine the derivate superstructure configurations related to the Bi_2Se_3 lattice. We have fixed the position of bismuth atoms and let the code iterate over all the inequivalent supercell configurations with five atoms per unit cell. We have found six possible ordered configurations. The optimised Enumlib structures are shown in Appendix A. To avoid the tedious task of converging k-point grids for each different cell, we opted to use a fixed density of k-points. From the previous convergence tests, we established that 7000 k-points per reciprocal atom was a sufficiently large value for the alloys.[38]

Table 5.4 The six inequivalent supercell configurations found. The geometry optimized lattice parameters for structures found are indicated.

Structure	Chemical formula	a (Å)	c (Å)
str 1	Bi_2Se_3	4.053	26.945
str 2	$Bi_2Se_2Te_1$	4.117	27.803
str 3	$Bi_2Se_1Te_2$	4.173	28.995
str 4	$Bi_2Se_2Te_1$	4.124	27.593
str 5	$Bi_2Se_1Te_2$	4.184	28.479
str 6	Bi_2Te_3	4.243	29.583

The lattice parameters of the resulting structures were optimized using LDA with van der Waals correction. The supercells generated by Enumlib are neither rhombohedral cells nor hexagonal cells. We used following matrix transformations to obtain the lattice parameters a and c shown in table 5.4:

$$\mathbf{A} = \mathbf{M}\mathbf{a}, \tag{5.2}$$

where $\mathbf{A}$ is the Enumlib output, $\mathbf{M}$ is the transformation matrix, and $\mathbf{a}$ is the matrix of the lattice vectors of the Bi_2Se_3 rhombohedral cell given row-wise. We can obtain matrix $\mathbf{M}$ by inverting matrix $\mathbf{a}$:

$$\mathbf{M} = \mathbf{A}\mathbf{a}^{-1}. \tag{5.3}$$

Then, we determine the effective parameters matrix, $\mathbf{a}'$, from the optimised supercell $\mathbf{A}'$ and the matrix $\mathbf{M}$:

$$\mathbf{a}' = \mathbf{M}^{-1}\mathbf{A}'. \tag{5.4}$$

Finally, from matrix $\mathbf{a}'$, we calculate the lattice parameters using the relation 5.1.

We plotted the obtained lattice parameters (table 5.4) to understand how they vary with the tellurium concentration in the alloy. Preliminary results indicate that the lattice parameters do not deviate significantly from linearity, as shown in figures 5.14 and 5.15.

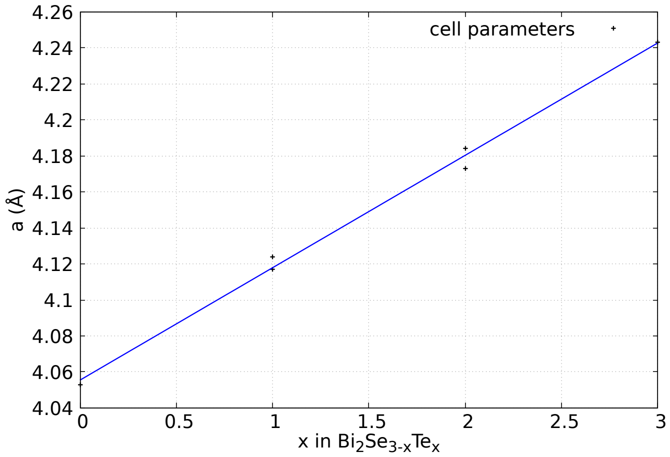

Fig. 5.14 Evolution of the *a* lattice parameter as a function of Te concentration, for the non-equivalent 5-atom ordered alloys. The fitting curve to the obtained lattice parameters is shown in blue.

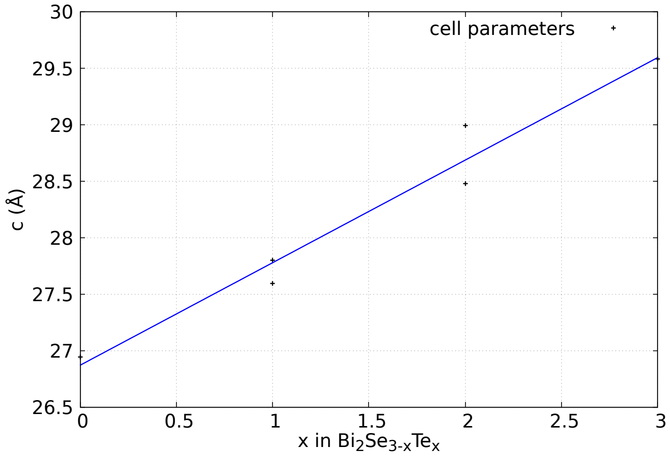

Fig. 5.15 Evolution of the *c* lattice parameter as a function of Te concentration, for the non-equivalent 5-atom ordered alloys. The fitting curve to the obtained lattice parameters is shown in blue.

Figures 5.16 to 5.21 show the calculated density of states with spin-orbit coupling for each configuration.

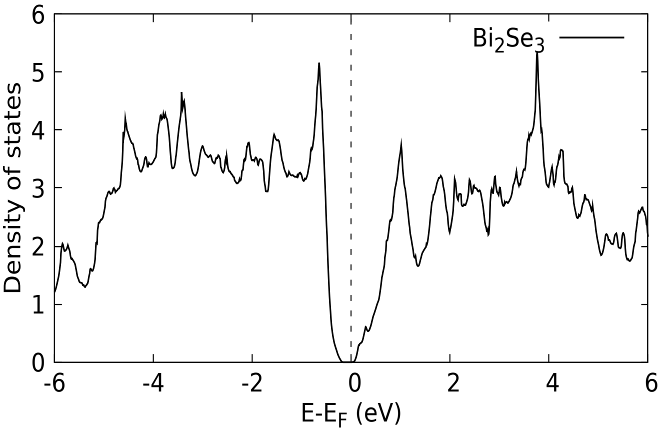

Fig. 5.16 Density of states for Bi_2Se_3 - str 1.

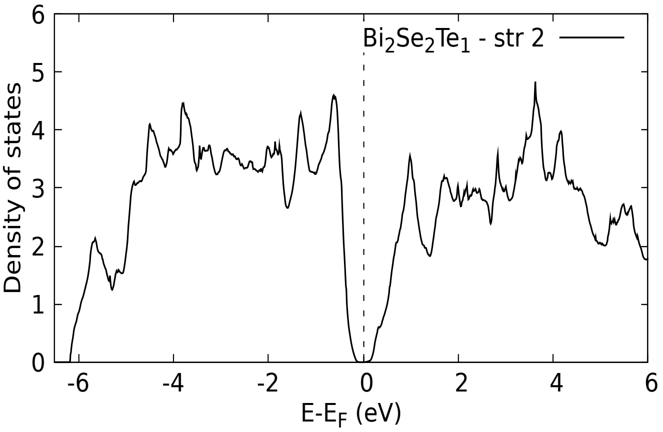

Fig. 5.17 Density of states for $Bi_2Se_2Te_1$ - str 2.

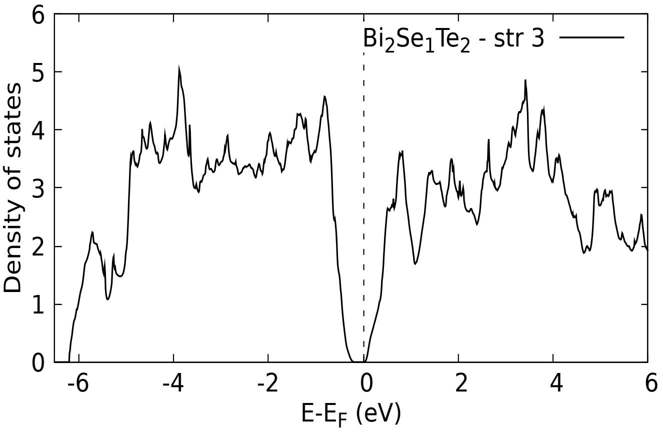

Fig. 5.18 Density of states for $Bi_2Se_1Te_2$ - str 3.

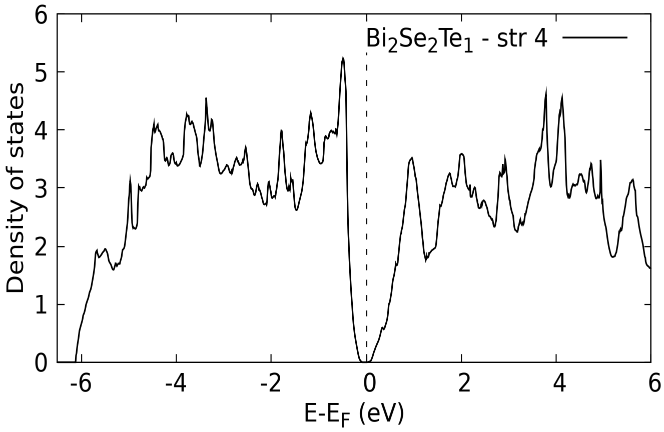

Fig. 5.19 Density of states for $Bi_2Se_2Te_1$ - str 4.

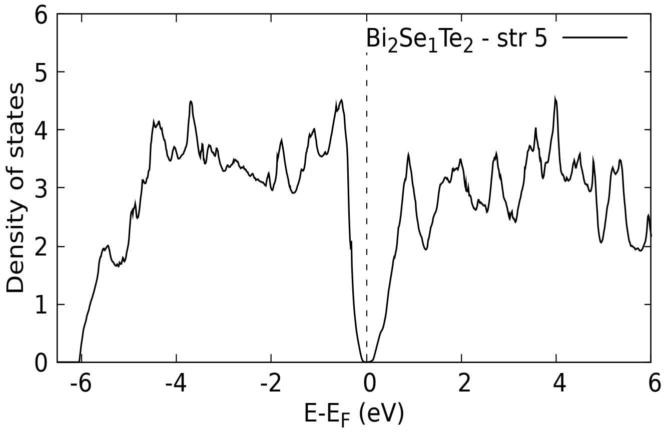

Fig. 5.20 Density of states for $Bi_2Se_1Te_2$ - str 5.

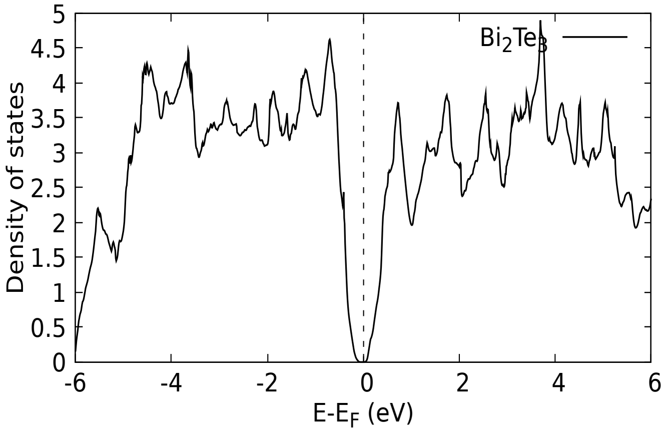

Fig. 5.21 Density of states for Bi_2Te_3 - str 6.

We obtained the conduction band minimum (CBM) and valence band maximum (VBM) for all ordered structures from the density of states calculations. The resulting band gaps are shown in table 5.5.

Table 5.5 Energy band gaps for the alloys' configurations

Chemical formula	Structure	E_{gap} (eV)
Bi_2Se_3	str 1	0.172
$Bi_2Se_2Te_1$	str 2	0.121
$Bi_2Se_2Te_1$	str 4	0.096
$Bi_2Se_1Te_2$	str 3	0.184
$Bi_2Se_1Te_2$	str 5	0.029
Bi_2Te_3	str 6	0.124

The energy gaps of the alloy systems indicate that the electronic structure strongly depends on the system's disorder, with the energy gaps of $Bi_2Se_1Te_2$ ranging from 0.03 eV to 0.18 eV. Further analysis of this strong dependency is necessary. Moreover, the band structures and the density of states yield different energy gaps for Bi_2Se_3 and Bi_2Te_3. We found that the conduction band minimum of Bi_2Se_3 is not located along the lines connecting high-symmetry points in the Brillouin zone.

According to the literature, the electronic structure calculations of the $Bi_2Se_{3-x}Te_x$ alloy systems are highly sensitive to the magnitude of the spin-orbit interaction. There is disagreement about where the CBM and the VBM are for Bi_2Te_3 and the ordered Bi_2SeTe_2. Recent studies indicate that for Bi_2Te_3 spin-orbit shifts the position of both CBM and VBM from the $Z - F$ line to a position within a plane that passes through Γ, Z and F in the Brillouin zone.[39]

We previously concluded that the band structure depends significantly on the lattice parameters and the exchange-correlation energy functionals. Furthermore, LDA with van der Waals correction adds over-binding to the system, increasing the spin-orbit coupling. Therefore, the results found concerning the energy gaps may arise from the complex interaction between the exchange-correlation energy functional, the geometry of the system, and the spin-orbit coupling.

5.4 $Bi_2Se_{2.5}Te_{0.5}$

One of the goals of this thesis was to give insight into the experimental results of our colleagues at CFisUc on the synthesis and characterisation of bismuth chalcogenides. They studied Bi_2Se_3, Bi_2Te_3 and three intermediate concentrations of alloy system: $Bi_2Se_{2.5}Te_{0.5}$, $Bi_2Se_{2.7}Te_{0.3}$, and $Bi_2Se_{2.9}Te_{0.1}$.[40] In this work, we study the alloy system with a tellurium concentration of $x = 0.5$ (10 atoms per unit cell). We choose this concentration since the other concentrations require considerably larger cells (50 atoms per unit cell), thus making the calculations much more expensive.

As previously, for the $Bi_2Se_{3-x}Te_x$ alloy system, we used the Enumlib code to find the 10-atom ordered structures corresponding to a concentration of tellurium of $x = 0.5$. Six structures corresponding to the distinct occupation of supercell's lattice sites by the tellurium atom were found - the numbers in table 5.6 label these structures. The optimised supercell configurations used are shown in Appendix A. A k-mesh density of 7000 k-points per atom was used in the following calculations.

Lattice parameters are obtained by optimising the Enumlib structures and converting the rhombohedral cells to hexagonal cells. The results are shown in table 5.6. It can be seen that the determined parameters fit the linear curve predicted for the alloy.

Table 5.6 Lattice parameters for ordered alloy structures at $Bi_2Se_{2.5}Te_{0.5}$ concentration.

Structure	a (Å)	c (Å)
str 7	4.080	27.539
str 8	4.086	27.382
str 15	4.086	27.330
str 16	4.089	27.262
str 43	4.080	27.330
str 47	4.084	27.327

To calculate the band structures, we used the primitive standard unit cells of the cells found. The k-path was selected according to Setyawan and Curtarolo[35]. The calculated band structures are shown in figures 5.22 to 5.27.

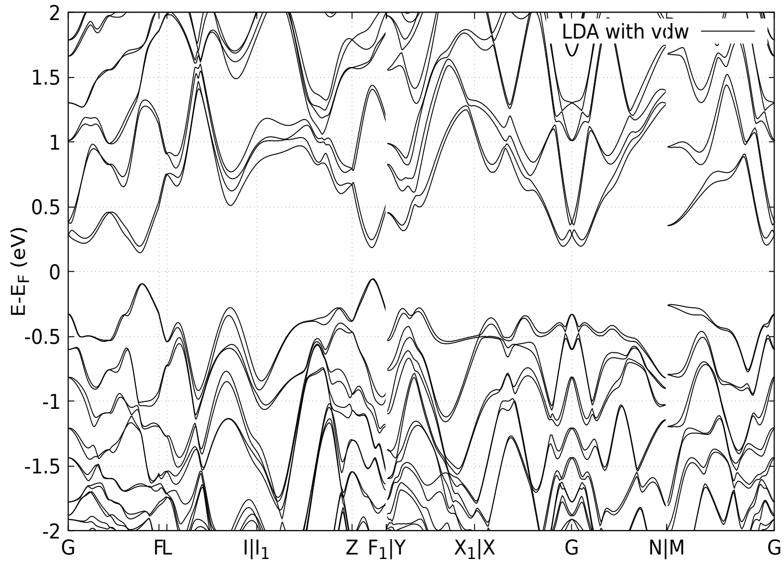

Fig. 5.22 Electronic band structure of structure 7 ordered alloy at $Bi_2Se_{2.5}Te_{0.5}$ concentration.

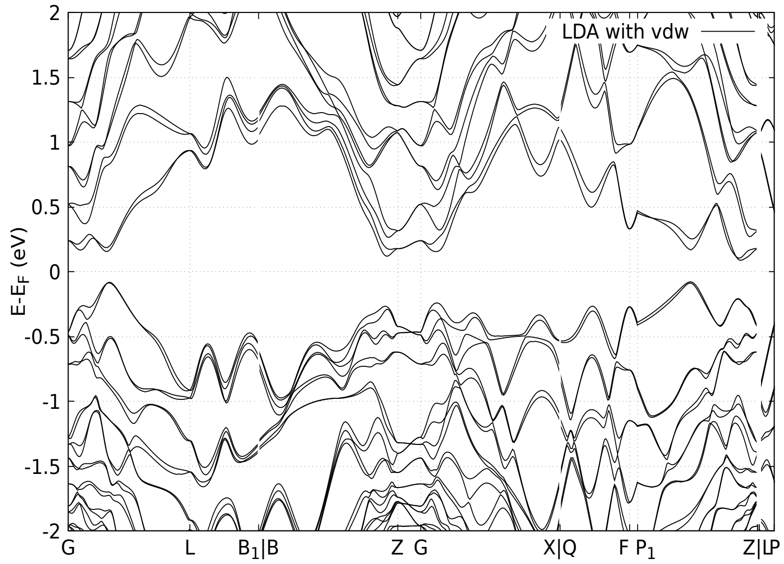

Fig. 5.23 Electronic band structure of structure 8 ordered alloy at $Bi_2Se_{2.5}Te_{0.5}$ concentration.

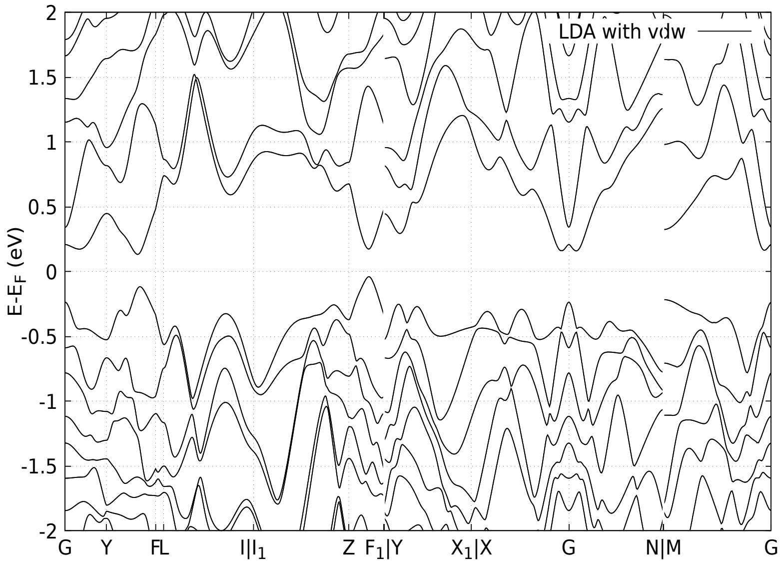

Fig. 5.24 Electronic band structure of structure 15 ordered alloy at $Bi_2Se_{2.5}Te_{0.5}$ concentration.

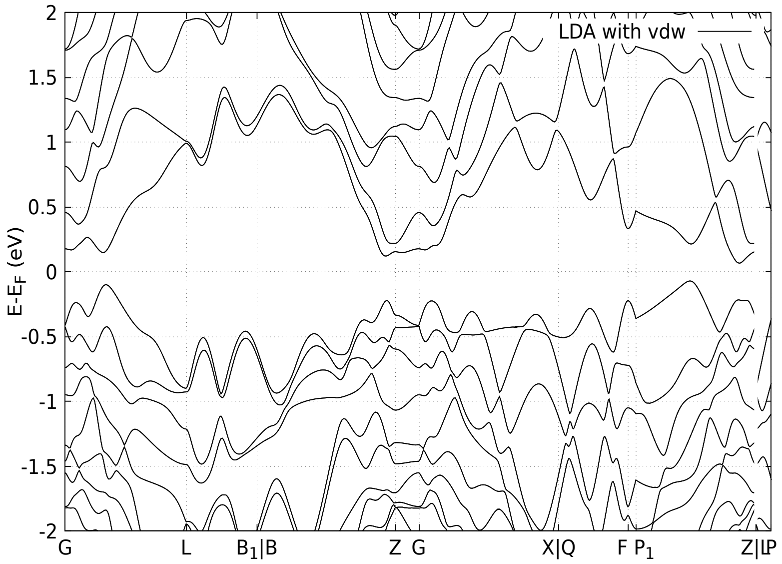

Fig. 5.25 Electronic band structure of structure 16 ordered alloy at $Bi_2Se_{2.5}Te_{0.5}$ concentration.

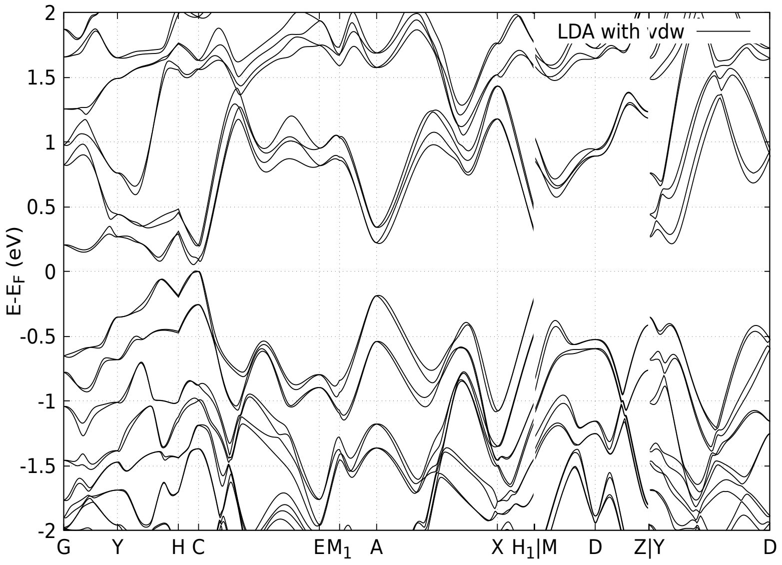

Fig. 5.26 Electronic band structure of structure 43 ordered alloy at $Bi_2Se_{2.5}Te_{0.5}$ concentration.

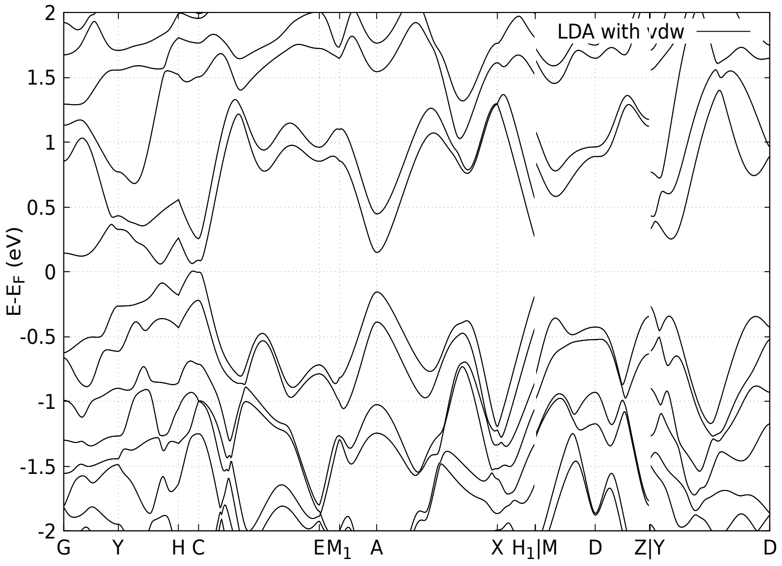

Fig. 5.27 Electronic band structure of structure 47 ordered alloy at $Bi_2Se_{2.5}Te_{0.5}$ concentration.

The band structure calculations of figures 5.26 and 5.27 show convergence problems due to depopulation of the correct valence level with the highest energy. As a result, the Fermi energy level is below the highest occupied valence band. Nevertheless, we determined the energy gap from the difference between the conduction band minimum and the valence band maximum. The table 5.7 shows the energy gaps obtained. The system's strong dependence on disorder supports the need for a more detailed analysis.

Table 5.7 Energy band gaps for ordered alloy structures at $Bi_2Se_{2.5}Te_{0.5}$ concentration.

Structure	E_{gap} (eV)
str 7	0.201
str 8	0.167
str 15	0.172
str 16	0.138
str 43	0.049
str 47	0.055

Chapter 6

Conclusions and future work

Based on the known topological and thermoelectric properties of $\mathrm{Bi_2Se_{3-x}Te_x}$, we proposed to model the alloy's energy bandgap, the lattice parameters, and the density of states.

By searching the exchange-correlation functional that provided an accurate description of the band structure, we find that the Van der Waals corrections are crucial to obtain lattice parameters and bandstructures that are in good agreement with the experimental results.

Preliminary calculations show that the lattice parameters of the alloy show no significant deviations from linearity.

Calculations of $\mathrm{Bi_2Se_3}$ show that spin-orbit coupling leads to changes in the conduction band minimum location, consistent with what has been described in the recent literature as a feature of the alloy. The change in the location of the band minimum to a point outside the lines connecting the high-symmetry points makes it difficult to model the system's electronic band structure and energy gap.

The ordered alloy (10-atom) supercells calculations for the $\mathrm{Bi_2Se_{2.5}Te_{0.5}}$ stoichiometry indicate that the electronic structure strongly depends on the system's disorder.

The values obtained are still preliminary to modelling the $\mathrm{Bi_2Se_{3-x}Te_x}$ alloy system. In the future, we hope to investigate better the position of the conduction band minimum as a function of the functional/geometry. In addition, we intend to refine the alloy's sampling by sampling more concentrations that require larger cells. Finally, we plan to study the evolution of other alloy properties, such as the topological indices, as a function of x.

References

[1] M. Z. Hasan and C. L. Kane. Colloquium: Topological insulators. *Reviews of Modern Physics*, 82(4):3045–3067, 2010. doi: 10.1103/revmodphys.82.3045.

[2] Haijun Zhang, Chao-Xing Liu, Xiao-Liang Qi, Xi Dai, Zhong Fang, and Shou-Cheng Zhang. Topological insulators in Bi2Se3, Bi2Te3 and Sb2Te3 with a single Dirac cone on the surface. *Nature Physics*, 5(6):438–442, 2009. doi: 10.1038/nphys1270.

[3] Xin Luo, Michael B. Sullivan, and Su Ying Quek. First-principles investigations of the atomic, electronic, and thermoelectric properties of equilibrium and strained Bi2Se3and Bi2Te3including van der Waals interactions. *Physical Review B*, 86(18), 2012. doi: 10.1103/physrevb.86.184111.

[4] S K Mishra, S Satpathy, and O Jepsen. Electronic structure and thermoelectric properties of bismuth telluride and bismuth selenide. *Journal of Physics: Condensed Matter*, 9(2): 461–470, 1997. doi: 10.1088/0953-8984/9/2/014.

[5] Ian Witting, Francesco Ricci, Thomas Chasapis, Geoffroy Hautier, and G. Snyder. The thermoelectric properties of n-type bismuth telluride: Bismuth selenide alloys $\mathrm{Bi_2Se_{3-x}Te_x}$. *Research*, 2020:1–15, 03 2020. doi: 10.34133/2020/4361703.

[6] Stefan Grimme. Semiempirical GGA-type density functional constructed with a long-range dispersion correction. *Journal of Computational Chemistry*, 27(15):1787–1799, 2006. doi: 10.1002/jcc.20495.

[7] P. Giannozzi et al. QUANTUM ESPRESSO: a modular and open-source software project for quantum simulations of materials. *Journal of Physics: Condensed Matter*, 21(39): 395502, 2009. doi: 10.1088/0953-8984/21/39/395502.

[8] P. Giannozzi et al. Advanced capabilities for materials modelling with Quantum ESPRESSO. *Journal of Physics: Condensed Matter*, 29(46):465901, 2017. doi: 10.1088/1361-648x/aa8f79.

[9] P. Hohenberg and W. Kohn. Inhomogeneous electron gas. *Phys. Rev.*, 136:B864–B871, Nov 1964. doi: 10.1103/PhysRev.136.B864. URL https://link.aps.org/doi/10.1103/PhysRev.136.B864.

[10] W. Kohn and L. J. Sham. Self-consistent equations including exchange and correlation effects. *Phys. Rev.*, 140:A1133–A1138, Nov 1965. doi: 10.1103/PhysRev.140.A1133. URL https://link.aps.org/doi/10.1103/PhysRev.140.A1133.

[11] Richard M. Martin. *Electronic Structure: Basic Theory and Practical Methods.* Cambridge University Press, 2004. doi: 10.1017/CBO9780511805769.

[12] W. Pauli. On the Connection between Spin and Statistics. *Progress of Theoretical Physics*, 5(4):526–543, 07 1950. ISSN 0033-068X. doi: 10.1143/ptp/5.4.526. URL https://doi.org/10.1143/ptp/5.4.526.

[13] Carlos Fiolhais, Fernando Nogueira, and Miguel Marques. *A Primer in Density Functional Theory (Lecture Notes in Physics, 620).* Springer, softcover reprint of the original 1st ed. 2003 edition, 2010.

[14] John P. Perdew. Jacob's ladder of density functional approximations for the exchange-correlation energy. *AIP Conference Proceedings*, 2001. doi: 10.1063/1.1390175.

[15] John P. Perdew, Adrienn Ruzsinszky, Jianmin Tao, Viktor N. Staroverov, Gustavo E. Scuseria, and Gábor I. Csonka. Prescription for the design and selection of density functional approximations: More constraint satisfaction with fewer fits. *The Journal of Chemical Physics*, 123(6):062201, 2005. doi: 10.1063/1.1904565.

[16] Marcel Franz and Laurens Molenkamp. *Topological Insulators (Volume 6) (Contemporary Concepts of Condensed Matter Science, Volume 6).* Elsevier, 1 edition, 2013.

[17] Neil Ashcroft and David Mermin. *Solid State Physics.* Cengage Learning, 1 edition, 1976.

[18] David Vanderbilt. *Berry Phases in Electronic Structure Theory: Electric Polarization, Orbital Magnetization and Topological Insulators.* Cambridge University Press, 1 edition, 2018.

[19] K. v. Klitzing, G. Dorda, and M. Pepper. New Method for High-Accuracy Determination of the Fine-Structure Constant Based on Quantized Hall Resistance. *Physical Review Letters*, 45(6):494–497, 1980. doi: 10.1103/physrevlett.45.494.

[20] David Tong. Lectures on the quantum hall effect, 2016. URL https://arxiv.org/abs/1606.06687.

[21] D. J. Thouless, M. Kohmoto, M. P. Nightingale, and M. den Nijs. Quantized Hall Conductance in a Two-Dimensional Periodic Potential. *Physical Review Letters*, 49(6): 405–408, 1982. doi: 10.1103/physrevlett.49.405.

[22] F. D. M. Haldane. Model for a Quantum Hall Effect without Landau Levels: Condensed-Matter Realization of the "Parity Anomaly". *Physical Review Letters*, 61(18):2015–2018, 1988. doi: 10.1103/physrevlett.61.2015.

[23] C. L. Kane and E. J. Mele. Quantum Spin Hall Effect in Graphene. *Physical Review Letters*, 95(22), 2005. doi: 10.1103/physrevlett.95.226801.

[24] Easo P. George, Dierk Raabe, and Robert O. Ritchie. High-entropy alloys. *Nature Reviews Materials*, 4(8):515–534, 2019. doi: 10.1038/s41578-019-0121-4.

[25] Marius Grundmann. *The Physics of Semiconductors.* Springer Publishing, New York, United States, 2018.

[26] Voicu Popescu and Alex Zunger. Effective Band Structure of Random Alloys. *Physical Review Letters*, 104(23), 2010. doi: 10.1103/physrevlett.104.236403.

[27] A. van de Walle, M. Asta, and G. Ceder. The alloy theoretic automated toolkit: A user guide. *Calphad*, 26(4):539–553, 2002. doi: 10.1016/s0364-5916(02)80006-2.

[28] Gus L. W. Hart and Rodney W. Forcade. Algorithm for generating derivative structures. *Physical Review B*, 77(22), 2008. doi: 10.1103/physrevb.77.224115.

[29] Xi Xu and Hong Jiang. Cluster expansion based configurational averaging approach to bandgaps of semiconductor alloys. *The Journal of Chemical Physics*, 150(3):034102, 2019. doi: 10.1063/1.5078399.

[30] L. Bellaiche and David Vanderbilt. Virtual crystal approximation revisited: Application to dielectric and piezoelectric properties of perovskites. *Physical Review B*, 61(12): 7877–7882, 2000. doi: 10.1103/physrevb.61.7877.

[31] J.M. Sanchez, F. Ducastelle, and D. Gratias. Generalized cluster description of multicomponent systems. *Physica A: Statistical Mechanics and its Applications*, 128(1-2):334–350, 1984. doi: 10.1016/0378-4371(84)90096-7.

[32] C. Sutton, S. Rigamonti, and M. Troppenz. Hands-On Tutorial on Cluster Expansion: Modeling of configurational energetics, 05 2016. URL https://th.fhi-berlin.mpg.de/sitesub/meetings/DFT-workshop-2016/uploads/Meeting/Tutorial_7_2016.pdf.

[33] Anubhav Jain, Shyue Ping Ong, Geoffroy Hautier, Wei Chen, William Davidson Richards, Stephen Dacek, Shreyas Cholia, Dan Gunter, David Skinner, Gerbrand Ceder, and Kristin A. Persson. Commentary: The materials project: A materials genome approach to accelerating materials innovation. *APL Materials*, 1(1):011002, 2013. doi: 10.1063/1.4812323.

[34] Seizo Nakajima. The crystal structure of $Bi_2Te_{3-x}Se_x$. *Journal of Physics and Chemistry of Solids*, 24(3):479–485, 1963. doi: 10.1016/0022-3697(63)90207-5.

[35] Wahyu Setyawan and Stefano Curtarolo. Setyawan, w. & curtarolo, s. high-throughput electronic band structure calculations: Challenges and tools. comput. mater. sci. 49, 299. *Computational Materials Science*, 49, 04 2010. doi: 10.1016/j.commatsci.2010.05.010.

[36] D.L. Greenaway and G. Harbeke. Band structure of bismuth telluride, bismuth selenide and their respective alloys. *Journal of Physics and Chemistry of Solids*, 26(10):1585–1604, 1965. doi: 10.1016/0022-3697(65)90092-2.

[37] J. Black, E.M. Conwell, L. Seigle, and C.W. Spencer. Electrical and optical properties of some m2v-bn3vi-b semiconductors. *Journal of Physics and Chemistry of Solids*, 2(3): 240–251, 1957. ISSN 0022-3697. doi: 10.1016/0022-3697(57)90090-2.

[38] Anubhav Jain, Geoffroy Hautier, Charles Moore, Shyue Ong, Christopher Fischer, Tim Mueller, Kristin Persson, and Gerbrand Ceder. A high-throughput infrastructure for density functional theory calculations. *Computational Materials Science - COMPUT MATER SCI*, 50:2295–2310, 06 2011. doi: 10.1016/j.commatsci.2011.02.023.

[39] Ian T. Witting, Thomas C. Chasapis, Francesco Ricci, Matthew Peters, Nicholas A. Heinz, Geoffroy Hautier, and G. Jeffrey Snyder. The thermoelectric properties of bismuth telluride. *Advanced Electronic Materials*, 5(6):1800904, 2019. doi: /10.1002/aelm.201800904.

[40] Vanda Marisa Mota Pereira. *Synthesis and transport properties of nanostructured topological insulators.* PhD thesis, 2016.

Appendix A

Optimised structures

$\mathbf{Bi_2Se_{3-x}Te_x}$:

- Bi_2Se_3 - structure 1:

```
CELL_PARAMETERS (angstrom)
   0.814698979  -3.970315324  -0.000003434
   0.000012550   2.068746859  -3.485315645
   8.464904272   3.805783553  -0.097695714

ATOMIC_POSITIONS (crystal)
Bi            0.4021369456        0.5978631306        0.2064113240
Bi            0.5978629964        0.4021368694        0.7935886180
Se            0.0000000000        0.0000000000        0.0000000000
Se            0.7937565213        0.2062435740        0.3812660910
Se            0.2062434437        0.7937564340        0.6187338700
```

- $Bi_2Se_2Te_1$ - structure 2:

```
CELL_PARAMETERS (angstrom)
   0.827601456  -4.033245157   0.000008247
   0.000018567   2.101548167  -3.540548773
   8.738803345   3.894803361  -0.082239252

ATOMIC_POSITIONS (crystal)
Bi            0.3999333664        0.6000666251        0.1997985869
Bi            0.6031143664        0.3968855913        0.8093444797
Se            0.0027220528       -0.0027220531        0.0081653368
Se            0.7889404180        0.2110595839        0.3668175488
Te            0.2052897033        0.7947102608        0.6158739508
```

- $Bi_2Se_1Te_2$ - structure 3:

```
CELL_PARAMETERS (angstrom)
   0.838820858  -4.087923465   0.000012754
   0.000017364   2.130042209  -3.588545451
   9.121361516   4.001794536  -0.051187408

ATOMIC_POSITIONS (crystal)
Bi            0.3941724341        0.6058275967        0.1825112907
Bi            0.6058275079        0.3941724033        0.8174886513
Se            0.0000000000        0.0000000000        0.0000000000
Te            0.7887067283        0.2112934270        0.3661152573
Te            0.2112932367        0.7887065810        0.6338847037
```

- $Bi_2Se_2Te_1$ - structure 4:

```
CELL_PARAMETERS (angstrom)
   0.828984455  -4.039818338  -0.000023002
  -0.000001519   2.104941593  -3.546344418
   8.670060740   3.884041896  -0.092437375

ATOMIC_POSITIONS (crystal)
Bi            0.4080147944        0.5919843053        0.2240428573
Bi            0.5919851476        0.4080156947        0.7759570847
Se            0.7965851274        0.2034142538        0.3897578051
Se            0.2034148376        0.7965857542        0.6102421559
Te            0.0000000000        0.0000000000        0.0000000000
```

- $Bi_2Se_1Te_2$ - structure 5:

```
CELL_PARAMETERS (angstrom)
   0.841098425  -4.098820786  -0.000031062
  -0.000005362   2.135677171  -3.598146958
   8.953513887   3.972931155  -0.074675628

ATOMIC_POSITIONS (crystal)
Bi            0.4057830316        0.5942169467        0.2173448479
Bi            0.5969441362        0.4030558566        0.7908413401
Se            0.7921976685        0.2078023073        0.3765953380
Te            0.0030741045       -0.0030741244        0.0092167746
Te            0.2020009663        0.7979990218        0.6060016025
```

- Bi$_2$Te$_3$ - structure 6:

```
CELL_PARAMETERS (angstrom)
   0.852976560  -4.156634989  -0.000020972
  -0.000022292   2.165806856  -3.648899024
   9.307443927   4.075648871  -0.047984732

ATOMIC_POSITIONS (crystal)
Bi            0.4001622096        0.5998377385        0.2004912613
Bi            0.5998377324        0.4001622615        0.7995086807
Te            0.0000000000        0.0000000000        0.0000000000
Te            0.7923376971        0.2076622727        0.3770302073
Te            0.2076622679        0.7923377353        0.6229697537
```

$\mathbf{Bi_2Se_{2.5}Te_{0.5}}$:

Enumlib optimised unit cells:

- structure 7:

```
CELL_PARAMETERS (angstrom)
  -4.084426991   0.000000000   0.000000000
   0.000000000  -7.065255249  -0.003689267
  -2.042213496   1.182081324   9.180377370

ATOMIC_POSITIONS (crystal)
Bi            0.5996041200        0.8005180262        0.8007917600
Bi            0.1021380869        0.2983458157        0.7957238263
Bi            0.9009607174        0.7030309429        0.1980785651
Bi            0.4014003677        0.1963981558        0.1971992645
Se            0.0028982849        0.0009409869       -0.0057965698
Se            0.5014470859        0.4977905782       -0.0028941718
Se            0.6869518437        0.0996888058        0.6260963125
Se            0.1853989539        0.6094949686        0.6292020923
Se            0.3154864216        0.8952682100        0.3690271568
Te            0.8037141180        0.3985235099        0.3925717640
```

- structure 8:

```
CELL_PARAMETERS (angstrom)
  -2.042982987  -3.538550443   0.000000000
  -2.042982987  -1.179516814  18.254984420
  -4.085965974   0.000000000   0.000000000
```

```
ATOMIC_POSITIONS (crystal)
Bi            0.2028941832        0.3913174403        0.2028941832
Bi            0.6981039881        0.9056880258        0.6981039881
Bi            0.2977991931        0.1066024208        0.2977991931
Bi            0.8027561261        0.5917316218        0.8027561261
Se           -0.0016232250        0.0048696749       -0.0016232250
Se            0.5030402251        0.4908793248        0.5030402251
Se            0.8978466711        0.3064599767        0.8978466711
Se            0.3933358510        0.8199924370        0.3933358510
Se            0.6028808704        0.1913573888        0.6028808704
Te            0.1029661170        0.6911016491        0.1029661170
```

- structure 15:

```
CELL_PARAMETERS (angstrom)
  -4.089087835   0.000000000   0.000000000
   0.000000000  -7.074334524  -0.005501494
  -2.044543918   1.184966900   9.110847059

ATOMIC_POSITIONS (crystal)
Bi            0.6049135252        0.8056881915        0.7901729397
Bi            0.1102556583        0.2928065443        0.7794886734
Bi            0.8897443517        0.7071934557        0.2205112966
Bi            0.3950864848        0.1943118085        0.2098270303
Se            0.0000000000        0.0000000000        0.0000000000
Se            0.6952525254        0.1004738661        0.6094949492
Se            0.1900431210        0.6064937609        0.6199137580
Se            0.3047474846        0.8995261339        0.3905050208
Se            0.8099568890        0.3935062391        0.3800862120
Te            0.5000000000        0.5000000000        0.0000000000
```

- structure 16:

```
CELL_PARAMETERS (angstrom)
  -2.044394642  -3.540995499   0.000000000
  -2.044394642  -1.180331833  18.174800429
  -4.088789283   0.000000000   0.000000000

ATOMIC_POSITIONS (crystal)
Bi            0.2047961805        0.3856114484        0.2047961805
Bi            0.7002829816        0.8991510451        0.7002829816
Bi            0.2997170184        0.1008489449        0.2997170184
Bi            0.7952038195        0.6143885416        0.7952038195
Se            0.0000000000        0.0000000000        0.0000000000
Se            0.8997844708        0.3006465775        0.8997844708
```

```
Se            0.3953812285        0.8138563046        0.3953812285
Se            0.6046187715        0.1861436854        0.6046187715
Se            0.1002155292        0.6993534125        0.1002155292
Te            0.5000000000        0.5000000000        0.5000000000
```

- structure 43:

```
CELL_PARAMETERS (angstrom)
   2.042132206  -3.537076846   0.000000000
   2.031519503   1.172898369   9.166662409
  -6.118786841  -3.532683341   0.006927635

ATOMIC_POSITIONS (crystal)
Bi            0.5000000000        0.8023090662        0.1001513074
Bi           -0.0000000001        0.7937848245        0.5992773282
Bi            0.5000000002        0.1994402258        0.8948130709
Bi           -0.0000000002        0.1961134551        0.4030578301
Se            0.0000000002       -0.0006829184       -0.0036276942
Se            0.4999999998       -0.0083811923        0.5006781127
Se            0.0000000003        0.6297313303        0.2035721222
Se            0.4999999997        0.6252460370        0.7157675943
Se            0.0000000001        0.3704368817        0.7879182107
Te            0.5000000000        0.3920021703        0.2983920777
```

- structure 47:

```
CELL_PARAMETERS (angstrom)
   2.045157061  -3.542316049   0.000000000
   2.026364746   1.169922269   9.104301454
  -6.123437254  -3.535368256   0.013799657

ATOMIC_POSITIONS (crystal)
Bi            0.5000000003        0.7907134193        0.0896211254
Bi           -0.0000000002        0.7785874506        0.5979837786
Bi            0.4999999997        0.2092865507        0.9103788646
Bi            0.0000000002        0.2214125194        0.4020162114
Se            0.0000000000        0.0000000000        0.0000000000
Se            0.0000000002        0.6208375976        0.2035448927
Se            0.4999999998        0.6080911704        0.7060651821
Se           -0.0000000002        0.3791623724        0.7964550973
Se            0.5000000002        0.3919087996        0.2939348079
Te            0.5000000000        0.0000000000        0.5000000000
```

Primitive standard unit cells:

- structure 7:

```
CELL_PARAMETERS (angstrom)
   2.042213496   9.256167939   0.000000000
  -2.042213496   9.256167939   0.000000000
   0.000000000   0.905944576   7.006932979

ATOMIC_POSITIONS (crystal)
Bi            0.5996041200        0.5996041200        0.8005180262
Bi            0.1021380869        0.1021380869        0.2983458157
Bi            0.9009607175        0.9009607175        0.7030309429
Bi            0.4014003677        0.4014003677        0.1963981558
Se            0.0028982849        0.0028982849        0.0009409869
Se            0.5014470859        0.5014470859        0.4977905782
Se            0.6869518438        0.6869518438        0.0996888058
Se            0.1853989539        0.1853989539        0.6094949686
Se            0.3154864216        0.3154864216        0.8952682100
Te            0.8037141180        0.8037141180        0.3985235099
```

- structure 8:

```
CELL_PARAMETERS (angstrom)
  18.293051031  -2.042983011   0.000000000
  18.293051031   2.042983011   0.000000000
  18.064889005   0.000000000   3.531186888

ATOMIC_POSITIONS (crystal)
Bi            0.7971058134        0.7971058134        0.7971058134
Bi            0.3018960086        0.3018960086        0.3018960086
Bi            0.7022008069        0.7022008069        0.7022008069
Bi            0.1972438739        0.1972438739        0.1972438739
Te            0.8970338830        0.8970338830        0.8970338830
Se            0.0016232249        0.0016232249        0.0016232249
Se            0.4969597749        0.4969597749        0.4969597749
Se            0.1021533255        0.1021533255        0.1021533255
Se            0.6066641456        0.6066641456        0.6066641456
Se            0.3971191296        0.3971191296        0.3971191296
```

- structure 15:

```
CELL_PARAMETERS (angstrom)
   2.044726943   9.188117238  -0.000045731
  -2.044726943   9.188117238  -0.000045731
```

```
   0.000000000   0.917885060   7.015025873

ATOMIC_POSITIONS (crystal)
Bi            0.6049089138        0.6049089138        0.8057111376
Bi            0.1102539263        0.1102539263        0.2927579152
Bi            0.8897460737        0.8897460737        0.7072420848
Bi            0.3950910862        0.3950910862        0.1942888624
Te            0.5000000000        0.5000000000        0.5000000000
Se            0.0000000000        0.0000000000        0.0000000000
Se            0.6952639578        0.6952639578        0.1005146832
Se            0.1900532825        0.1900532825        0.6064592343
Se            0.3047360422        0.3047360422        0.8994853168
Se            0.8099467175        0.8099467175        0.3935407657
```

- structure 16:

```
CELL_PARAMETERS (angstrom)
  18.213087432  -2.044394665   0.000000000
  18.213087432   2.044394665   0.000000000
  17.983606870   0.000000000   3.533551657

ATOMIC_POSITIONS (crystal)
Bi            0.7952038161        0.7952038161        0.7952038161
Bi            0.2997170150        0.2997170150        0.2997170150
Bi            0.7002829850        0.7002829850        0.7002829850
Bi            0.2047961839        0.2047961839        0.2047961839
Te            0.5000000000        0.5000000000        0.5000000000
Se            0.0000000000        0.0000000000        0.0000000000
Se            0.1002155258        0.1002155258        0.1002155258
Se            0.6046187682        0.6046187682        0.6046187682
Se            0.3953812318        0.3953812318        0.3953812318
Se            0.8997844742        0.8997844742        0.8997844742
```

- structure 43:

```
CELL_PARAMETERS (angstrom)
   4.084264507   0.000000000   0.000000000
   0.000000000   7.065369911   0.000000000
   0.000000000   2.336807591   9.168958069

ATOMIC_POSITIONS (crystal)
Bi            0.5000000000        0.1001513074        0.1976909338
Bi            0.0000000000        0.5992773282        0.2062151755
Bi            0.5000000000        0.8948130709        0.8005597742
Bi            0.0000000000        0.4030578301        0.8038865449
```

```
Te            0.5000000000        0.2983920777        0.6079978297
Se            0.0000000000        0.9963723058        0.0006829184
Se            0.5000000000        0.5006781127        0.0083811923
Se            0.0000000000        0.2035721222        0.3702686697
Se            0.5000000000        0.7157675943        0.3747539630
Se            0.0000000000        0.7879182107        0.6295631183
```

- structure 47:

```
CELL_PARAMETERS (angstrom)
   4.090314217   0.000000000   0.000000000
   0.000000000   7.070749815   0.000000000
   0.000000000   2.322071580   9.108850682

ATOMIC_POSITIONS (crystal)
Bi            0.5000000000        0.0896211254        0.2092865807
Bi            0.0000000000        0.5979837786        0.2214125494
Bi            0.5000000000        0.9103788746        0.7907134193
Bi            0.0000000000        0.4020162214        0.7785874506
Te            0.5000000000        0.5000000000        0.0000000000
Se            0.0000000000        0.0000000000        0.0000000000
Se            0.0000000000        0.2035448927        0.3791624024
Se            0.5000000000        0.7060651821        0.3919088296
Se            0.0000000000        0.7964551073        0.6208375976
Se            0.5000000000        0.2939348179        0.6080911704
```